axioms

MDPI

Article

Shock Mach Number Effect on Instability Evolution at a Light–Heavy Fluid Interface: A Numerical Investigation

Salman Saud Alsaeed [1], Satyvir Singh [2,3,*] and Nahar F. Alshammari [4]

[1] Department of Mathematics, College of Science, Jouf University, P.O. Box 2014, Sakaka 72388, Saudi Arabia; ssalsaeed@ju.edu.sa
[2] Institute of Applied and Computational Mathematics, RWTH Aachen University, 52062 Aachen, Germany
[3] Department of Mathematics, Graphic Era Deemed to be University, Dehradun 248002, India
[4] Department of Electrical Engineering, College of Engineering, Jouf University, P.O. Box 2014, Sakaka 72388, Saudi Arabia; nfalshamari@ju.edu.sa
* Correspondence: singh@acom.rwth-aachen.de; Tel.: +49-162-4707-356

Abstract

Shock–accelerated interfaces between fluids of different densities are prone to Richtmyer–Meshkov-type instabilities, whose evolution is strongly influenced by the incident shock Mach number. In this study, we present a systematic numerical investigation of the Mach number effect on the instability growth at a light–heavy fluid layer. The governing dynamics are modeled using the compressible multi-species Euler equations, and the simulations are performed with a high-order modal discontinuous Galerkin method. This approach provides accurate resolution of sharp interfaces, shock waves, and small-scale vortical structures. A series of two-dimensional simulations is carried out for a range of shock Mach numbers impinging on a sinusoidally perturbed light–heavy fluid interface. The results highlight the distinct stages of instability evolution, from shock–interface interaction and baroclinic vorticity deposition to nonlinear roll-up and interface deformation. Quantitative diagnostics—including circulation, enstrophy, vorticity extrema, and mixing width—are employed to characterize the instability dynamics and to isolate the role of Mach number in enhancing or suppressing growth. Particular attention is given to the mechanisms of vorticity generation through baroclinic torque and compressibility effects. Moreover, the analysis of controlling parameters, including Atwood number, layer thickness, and initial perturbation amplitude, broadens the parametric understanding of shock-driven instabilities. The results reveal that increasing shock Mach number markedly enhances vorticity generation and accelerates interface growth, while the resulting nonlinear morphology remains strongly sensitive to variations in Atwood number and perturbation amplitude.

Keywords: shock-accelerated instability; mach number effect; light–heavy fluid layer; shock-driven mixing; shock–vortex interaction; baroclinic vorticity generation; interface morphology

MSC: 76E19; 35Q31; 76M22; 76-10

Academic Editor: Angel Ricardo Plastino

Received: 8 September 2025
Revised: 13 October 2025
Accepted: 30 October 2025
Published: 31 October 2025

Citation: Alsaeed, S.S.; Singh, S.; Alshammari, N.F. Shock Mach Number Effect on Instability Evolution at a Light–Heavy Fluid Interface: A Numerical Investigation. *Axioms* **2025**, *14*, 813. https://doi.org/10.3390/axioms14110813

1. Introduction

Shock-accelerated interfacial instabilities occur when a shock wave interacts with a perturbed density interface between two fluids of different densities [1]. The impulsive deposition of vorticity due to misaligned pressure and density gradients drives perturbation growth, leading to complex nonlinear structures and eventual turbulent mixing.

This class of instabilities, collectively associated with the Richtmyer–Meshkov instability (RMI) [2,3], is of central importance in high-energy-density physics, astrophysical flows, and engineering systems [4–8]. For example, in inertial confinement fusion (ICF), shock–interface interactions control fuel–ablator mixing and influence ignition efficiency [9]. In astrophysics, RMI plays a role in supernova remnants, where shock waves interact with stratified stellar material [10]. Similarly, in supersonic combustion and scramjet propulsion, shock-induced mixing enhances combustion but may also cause unwanted flow destabilization [11–13]. These broad applications motivate careful numerical and experimental studies of the underlying physics [14].

The canonical mechanism of RMI begins when a shock crosses a perturbed density interface, imparting an impulsive acceleration [7]. This acceleration generates a vorticity sheet at the interface through the baroclinic torque, which arises from the non-parallel alignment of pressure and density gradients. The deposited vorticity drives the interface to grow, forming spikes of the heavy fluid penetrating into the light fluid and bubbles of the light fluid rising into the heavy fluid [15,16]. Over time, secondary Kelvin–Helmholtz instabilities (KHI) develop due to shear along the interface, rolling up vortical structures and accelerating mixing. Depending on shock strength and interface characteristics, the instability may evolve from an initial linear regime to nonlinear growth and eventually to a turbulent mixing layer [17,18]. Understanding these distinct stages is crucial for predictive modeling of instability dynamics.

Among the many parameters influencing RMI, the shock Mach number plays a decisive role in determining instability evolution. The Mach number governs the strength of pressure loading and, therefore, the magnitude of vorticity deposition [19,20]. At low Mach numbers, the interface perturbations grow relatively slowly and the instability remains in the quasi-linear regime for extended durations [21]. At higher Mach numbers, vorticity deposition is amplified, leading to strong circulation growth, faster spike/bubble development, and accelerated transition into the nonlinear stage [22,23]. Moreover, shock focusing and compression waves at higher Mach numbers significantly alter pressure distribution and density gradients, further enhancing instability growth [23]. However, the detailed dependence of instability morphology and diagnostics on Mach number remains incompletely characterized, particularly for finite-thickness layers.

Most prior studies have focused on simplified interface geometries, such as single sharp interfaces, shocked bubbles, or planar curtains [24–28]. While these studies have advanced theoretical understanding and provided benchmarks for numerical validation, they often neglect the finite thickness of realistic fluid layers [29,30]. In practice, density interfaces are rarely discontinuous but instead transition across a finite distance due to diffusion, ablation, or preparation conditions. For example, in gas curtain experiments, the curtain thickness introduces an additional physical length scale that modifies wave interactions and instability growth [31]. Similarly, in ICF capsules, the ablator–fuel interface is diffuse rather than sharp, altering acoustic transit times and mode synchronization [32]. Recently, Alsaeed et al. [33,34] numerically and systematically analyzed the influence of Atwood number and layer thickness on shock-driven interfacial instabilities. Their findings revealed that increasing Atwood number amplifies baroclinic vorticity generation and accelerates nonlinear roll-up, while thinner heavy layers enhance circulation through stronger reverberations and earlier Kelvin–Helmholtz onset.

Experimental investigations have contributed significantly to our understanding of shock–interface interactions. Schlieren photography, particle image velocimetry, and X-ray diagnostics have provided valuable visualizations of shock-driven mixing [35,36]. However, experimental setups face limitations: precise control of initial perturbations is difficult, shock Mach number cannot always be varied systematically, and measurements of

fine-scale vortical structures or enstrophy remain challenging. In contrast, numerical simulations provide full spatiotemporal resolution of flow fields, enabling systematic parametric studies while isolating individual physical mechanisms [1,37]. With increasing computational resources, high-fidelity simulations have become indispensable for complementing experimental data and guiding theoretical development.

A variety of numerical frameworks have been employed to study RMI, including finite-difference, finite-volume, spectral, and lattice-Boltzmann methods [38–40]. However, capturing both sharp shock waves and smooth vortical structures requires schemes that combine robustness with high accuracy. High-order discontinuous Galerkin (DG) methods have emerged as particularly attractive due to their spectral-like convergence, local conservation, and suitability for unstructured meshes [41–43]. Modal DG schemes, which employ orthogonal polynomial bases, are especially effective in resolving multi-scale dynamics. When coupled with appropriate Riemann solvers and limiters, DG methods accurately capture shocks while maintaining high-order accuracy in smooth regions. These capabilities make DG methods ideally suited for shock–interface interaction studies.

Recent experimental and computational studies have significantly advanced the understanding of complex shock–vortex and shock-train dynamics in compressible flows. Wang et al. [44] conducted detailed visualizations and analyses of shock-wave–streamwise-vortex interactions, whereas Wang et al. [45] examined the evolution of shock trains in concave channels using combined experimental and numerical methods. Tang et al. [46] developed a hybrid RANS–LES framework with adaptive grid refinement for rotor–stator interactions, achieving improved predictive accuracy for unsteady compressible flows. In related efforts, Zheng et al. [47] applied reinforcement-learning-based plasma actuation to suppress asymmetric vortex structures in high-angle-of-attack flows. Further, Fujio and Ogawa [48] advanced numerical modeling of shock-driven interfacial flows by formulating an adaptive mesh refinement approach capable of accurately capturing both shock and interface dynamics in compressible multi-material systems. Peng and Chen [49] employed large-eddy simulations to demonstrate how alternating-wedge strut hypermixers enhance fuel–air mixing in Mach 3.5 supersonic flows, showing that larger trailing-edge ramp and injection angles significantly improve mixing efficiency while maintaining flow stability. Collectively, these studies highlight emerging strategies for the modeling, prediction, and control of shock-induced instabilities. Building upon these advances, the present work focuses on the Mach number effect on instability evolution at a light–heavy fluid interface, offering complementary insights into baroclinic vorticity generation and interface deformation mechanisms.

The present study employs a high-order modal DG solver to investigate the influence of shock Mach number on instability evolution at a light–heavy fluid interface. The governing equations are the compressible multi-species Euler equations, which neglect viscous dissipation but capture the essential mechanisms of compressibility and baroclinic vorticity generation. This formulation isolates the Mach number effect by eliminating additional complexities such as viscosity, bulk diffusion, or thermal non-equilibrium. The DG framework enables accurate tracking of interface morphology, shock propagation, and small-scale vortical structures, providing high-fidelity data for systematic analysis.

In the numerical setup, a sinusoidally perturbed light–heavy fluid layer is subjected to incident planar shocks of varying Mach numbers. This configuration allows us to isolate the impact of shock strength on instability growth while retaining the essential physics of a stratified layer. Diagnostics such as interface amplitude, circulation, vorticity extrema, enstrophy, and mixing width are extracted to quantify the instability dynamics. By comparing across Mach numbers, we highlight how shock strength modifies both the linear and nonlinear stages of instability evolution. Particular emphasis is placed on the mechanisms

of vorticity generation. Through analysis of the vorticity transport equation, we decompose contributions from baroclinic torque, compressibility effects, and flow dilatation. This decomposition clarifies the physical pathways by which shock strength modulates vorticity deposition and subsequent instability growth. In addition, interface morphology is examined to identify how Mach number influences bubble flattening, spike sharpening, and vortex roll-up. Such detailed analysis is essential for developing reduced-order models and scaling laws that predict instability growth across a range of flow conditions.

The remainder of this paper is organized as follows. Section 2 presents the governing equations and physical model. Section 3 details the numerical methodology, including the high-order modal DG framework and validation procedures. Section 4 describes the problem setup, including the fluid configuration, Atwood number range, Mach numbers considered, and initial perturbations. Section 5 presents the results and discusses them, with subsections devoted to flow field evolution, vorticity dynamics, quantitative diagnostics, and interface morphology. Finally, Section 6 summarizes the main findings, discusses implications for shock-driven mixing, and outlines directions for future research.

2. Physical Problem Description

Figure 1 illustrates the two-dimensional configuration adopted to investigate the influence of shock Mach number on instability evolution across a light–heavy gas layer. The computational domain is a rectangular region of size $[0, 100] \times [0, 200]$ mm^2 in the (x, y) plane. A finite-thickness heavy-gas layer (SF_6) of thickness $d = 10$ mm is embedded within an ambient light gas (N_2), forming a canonical light–heavy–light stratification. The layer is bounded upstream by a sinusoidally perturbed interface I_1 and downstream by a planar interface I_2. The upstream interface I_1 is initialized with a single-mode sinusoidal perturbation defined as $x = a_0 \cos(2\pi y/\lambda)$, where a_0 and λ denote the initial perturbation amplitude and wavelength, respectively. In all simulations, the amplitude and wavelength are fixed at $a_0 = 40$ mm and $\lambda = 100$ mm. The downstream interface I_2 remains planar, providing a reference surface for assessing transmitted and reflected wave interactions within the heavy layer.

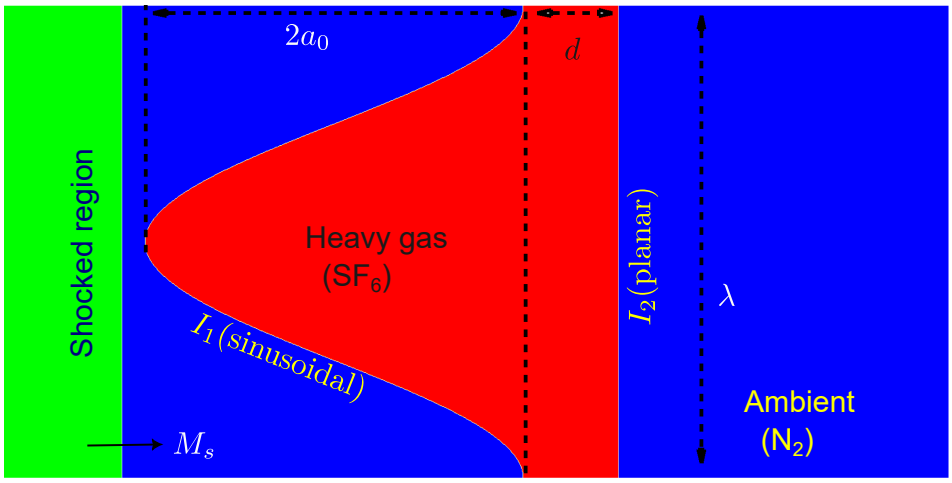

Figure 1. Schematic of the computational setup for shock–interface interaction in a two-dimensional light–heavy gas configuration. A planar shock of Mach number $M_s = 1.15$–2.0 propagates from left to right through the ambient light gas (N_2) and impinges on the sinusoidally perturbed upstream interface I_1 of the heavy-gas (SF_6) layer. The perturbation has initial amplitude a_0 and wavelength λ. The heavy layer has finite thickness d, bounded downstream by a planar interface I_2.

A planar incident shock (IS) is initialized in the ambient gas and propagates in the positive x-direction. At $t = 0$, the IS front is positioned 25 mm from the left boundary, while

the leftmost crest of the perturbed interface I_1 lies 5 mm downstream of the shock front. This placement ensures that the shock first interacts with the sinusoidal interface, initiating RMI through baroclinic vorticity deposition. The strength of the IS is characterized by the incident Mach number M_s. To isolate the effect of shock strength, five Mach numbers are considered: $M_s = 1.15$, 1.25, 1.50, 1.75, and 2.00. The perturbation amplitude, wavelength, and heavy-layer thickness are kept constant at $a_0 = 40$ mm, $\lambda = 100$ mm, and $d = 10$ mm, respectively. This approach enables systematic examination of how shock strength alone influences vorticity generation, interface deformation, and instability growth dynamics.

The density contrast between the heavy and light gases is characterized by the Atwood number, defined as

$$A = \frac{\rho_h - \rho_l}{\rho_h + \rho_l}, \tag{1}$$

where ρ_h and ρ_l represent the densities of the heavy gas (SF_6) and light gas (N_2), respectively. In the present configuration, the Atwood number is $A = 0.66 > 0$, corresponding to a stratification in which the heavier gas layer is embedded between lighter ambient regions. Such a positive Atwood number denotes a dynamically unstable arrangement that serves as a canonical setup for investigating shock-driven interfacial instabilities and mixing phenomena. The thermophysical properties of the gas pair used in the simulations are listed in Table 1. The quantities include the ratio of specific heats (γ), density (ρ), specific heat at constant pressure (C_p), and molecular weight (M), all evaluated at the initial reference state.

Table 1. Thermophysical properties of the gas pair used in this study at the $P_0 = 101{,}325$ Pa and $T_0 = 293$ K.

Gas	Heat Ratio (γ)	Density ($\mathbf{g\,cm^{-3}}$)	Specific Heat ($\mathbf{kJ\,g^{-1}\,K^{-1}}$)	Molecular Weight ($\mathbf{g\,mol^{-1}}$)
N_2	1.40	1.25×10^{-3}	1.04×10^{-3}	28.0134
SF_6	1.09	6.03×10^{-3}	0.656×10^{-3}	128.491

3. Mathematical Formulation

The instability dynamics considered in this work are governed by the two-dimensional compressible Euler equations for two-component gas mixtures. These equations provide a conservative description of shock–interface interactions in immiscible flows, where baroclinic torque is the dominant mechanism for vorticity generation. Viscous, diffusive, and conductive processes are neglected to isolate the role of shock Mach number in driving instability evolution. In the following, the governing equations, interface representation, non-dimensional parameters, vorticity transport formulation, and modeling assumptions are described in detail.

3.1. Compressible Euler Equations for Two-Component Gas Flows

The system is modeled as a binary, ideal, non-reactive gas mixture described by the conservation of mass, momentum, energy, and species mass fractions. The conserved state vector is defined as

$$\mathbf{U} = \begin{bmatrix} \rho \\ \rho u \\ \rho v \\ \rho E \\ \rho Y_k \end{bmatrix}, \tag{2}$$

where ρ is the mixture density, (u, v) are the velocity components in the x- and y-directions, E is the specific total energy, and Y_k is the mass fraction of species k ($k = 1, 2$).

The governing equations are expressed in conservative form as

$$\frac{\partial \mathbf{U}}{\partial t} + \frac{\partial \mathbf{F}(\mathbf{U})}{\partial x} + \frac{\partial \mathbf{G}(\mathbf{U})}{\partial y} = 0, \tag{3}$$

where $\mathbf{F}$ and $\mathbf{G}$ denote the inviscid flux vectors in the x- and y-directions:

$$\mathbf{F}(\mathbf{U}) = \begin{bmatrix} \rho u \\ \rho u^2 + p \\ \rho uv \\ (\rho E + p)u \\ \rho Y_k u \end{bmatrix}, \qquad \mathbf{G}(\mathbf{U}) = \begin{bmatrix} \rho v \\ \rho uv \\ \rho v^2 + p \\ (\rho E + p)v \\ \rho Y_k v \end{bmatrix}. \tag{4}$$

The closure is provided by the ideal gas law

$$p = \rho R T, \qquad R = \sum_k Y_k R_k, \tag{5}$$

where $R_k = R_u / M_k$ is the specific gas constant of species k with molar mass M_k, and R_u is the universal gas constant.

The mixture total energy is given by

$$\rho E = \frac{p}{\bar{\gamma} - 1} + \tfrac{1}{2}\rho(u^2 + v^2), \tag{6}$$

with $\bar{\gamma}$ denoting the effective specific heat ratio, determined from mixture-averaged specific heats,

$$\bar{C}_p = \sum_k z_k C_{p,k}, \quad \bar{C}_v = \sum_k z_k C_{v,k}, \quad \bar{\gamma} = \frac{\bar{C}_p}{\bar{C}_v}, \quad z_k = \frac{Y_k}{M_k}. \tag{7}$$

For each species k, the calorically perfect gas assumption yields

$$C_{p,k} = \frac{\gamma_k R_u}{\gamma_k - 1}, \qquad C_{v,k} = C_{p,k} - R_u, \tag{8}$$

with γ_k the specific heat ratio of species k. Alternatively, the mixture pressure can be expressed using Dalton's law:

$$p = \sum_k p_k, \qquad p_k = \rho_k R_k T, \qquad \rho_k = \rho Y_k. \tag{9}$$

This formulation enables consistent representation of multi-species compressible flows and provides the foundation for analyzing Atwood number effects in shock–interface dynamics.

3.2. Initial and Boundary Conditions

A planar incident shock of prescribed strength, characterized by the Mach number M_s, is initialized in the ambient light gas and positioned upstream of the heavy layer. The unshocked region ahead of the shock maintains the uniform ambient state (p_0, ρ_0, T_0), where p_0 = 101,325 Pa and $T_0 = 273$ K are the initial pressure and temperature, respectively. The post-shock state, which occupies the region immediately behind the shock front, is obtained from the one-dimensional Rankine–Hugoniot (RH) jump conditions, derived from the conservation of mass, momentum, and total energy across a discontinuity

$$M_2^2 = \frac{2 + (\gamma - 1)M_s^2}{1 - \gamma + 2\gamma M_s^2}, \quad \frac{p_2}{p_1} = \frac{1 + \gamma M_s^2}{1 + \gamma M_2^2}, \quad \frac{\rho_2}{\rho_1} = \frac{\gamma - 1 + (\gamma + 1)\, p_2/p_1}{\gamma + 1 + (\gamma - 1)\, p_2/p_1}. \tag{10}$$

Here, subscripts 1 and 2 denote the pre-shock and post-shock states, respectively. The parameter $\gamma = c_p/c_v$ is the specific heat ratio for the corresponding gas, taken as $\gamma = 1.4$ for nitrogen in the present configuration. M_s is the incident shock Mach number, and M_2 represents the post-shock Mach number determined from the RH relations.

The computed post-shock conditions are imposed at the left inflow boundary to maintain a planar shock of the desired strength throughout the simulation. Non-reflecting boundary conditions are applied at the right, top, and bottom boundaries to prevent spurious wave reflections. This setup ensures that the planar shock interacts cleanly with the perturbed upstream interface I_1 and propagates through the heavy-gas layer, allowing the investigation of Mach-number-dependent instability evolution without boundary interference.

3.3. Vorticity Transport Formulation

The generation and evolution of vorticity play a central role in shock-driven interfacial instabilities, as they directly govern the amplification of perturbations and the subsequent transition to nonlinear mixing. In compressible multi-species flows, the vorticity dynamics can be derived from the curl of the momentum equation. For a two-dimensional flow field, the spanwise vorticity is defined as

$$\omega = (\nabla \times \mathbf{u})_z = \frac{\partial v}{\partial x} - \frac{\partial u}{\partial y}, \tag{11}$$

where (u, v) are the velocity components in the x- and y-directions. The corresponding vorticity transport equation takes the form

$$\frac{D\omega}{Dt} = -\omega(\nabla \cdot \mathbf{u}) + \frac{1}{\rho^2}\nabla\rho \times \nabla p, \tag{12}$$

where $D/Dt = \partial/\partial t + \mathbf{u} \cdot \nabla$ is the material derivative. The right-hand side consists of two distinct contributions:

The first term, $-\omega(\nabla \cdot \mathbf{u})$, accounts for compressibility effects associated with flow dilatation. In regions of strong compression or expansion, this term can amplify or attenuate existing vorticity. Although it is generally weaker than the baroclinic contribution in shock–interface interactions, it becomes increasingly important at higher Mach numbers where compressibility effects are stronger. The second term, $(1/\rho^2)\nabla\rho \times \nabla p$, represents baroclinic torque. This term is non-zero only when the density and pressure gradients are misaligned, a condition naturally satisfied at a perturbed density interface impacted by a shock wave. The resulting vorticity sheet is the primary driver of instability growth in inviscid multi-species flows, giving rise to the characteristic spike and bubble structures of RMI.

In the present study, viscosity and diffusion are neglected, and hence vortex stretching and viscous dissipation terms are absent from Equation (12). This simplification isolates the fundamental mechanisms of vorticity generation in compressible flows, particularly the interplay between baroclinic torque and compressibility. The vorticity formulation also provides a natural framework for quantitative diagnostics. By examining spatial distributions of ω, as well as integral measures such as circulation and enstrophy, one can track the efficiency of vorticity deposition across different Mach numbers. Furthermore, decomposition of the production terms in Equation (12) allows direct assessment of how shock strength modulates the balance between baroclinic and compressibility-driven contributions. Such analysis is crucial for understanding the transition from linear growth to nonlinear roll-up in shock-accelerated interfaces.

3.4. Assumptions and Simplifications

The present model neglects viscosity, thermal conduction, and molecular diffusion, thereby restricting the analysis to inviscid, compressible dynamics. This assumption isolates the role of baroclinic torque and compressibility in driving vorticity generation, but it also precludes the representation of viscous dissipation, molecular diffusion, and three-dimensional vortex stretching. Consequently, while the results accurately capture early and intermediate stages of interface evolution, they should not be interpreted as modeling fully developed turbulent mixing.

Notably, the present inviscid Euler-based formulation differs from hybrid or viscous frameworks that include additional physical mechanisms. For instance, Tang et al. [46] developed a hybrid RANS–LES approach with adaptive mesh refinement for compressible rotor–stator interactions, demonstrating improved predictive fidelity for unsteady turbulent flows. Such methods explicitly account for viscous stresses, subgrid turbulence, and energy dissipation, but they also require more complex modeling assumptions and higher computational cost. In contrast, the inviscid approach used here serves to isolate the Mach-number-driven baroclinic processes that dominate the early stages of instability growth before viscous and diffusive effects become significant.

4. Numerical Methodology, Benchmarks, and Grid Resolution

Accurate numerical modeling of shock–interface interactions requires high-order discretization schemes that can capture both sharp discontinuities and small-scale vortical structures. To this end, the present study employs a high-order discontinuous Galerkin framework and validates its performance against well-documented experimental benchmarks before applying it to investigate Mach number effects on light–heavy fluid layers.

4.1. Numerical Methodology

The compressible multi-component Euler equations are solved using an in-house high-order discontinuous Galerkin (DG) solver [50]. The domain is discretized into Cartesian elements, with the solution in each element represented by third-order Legendre polynomials. Flux integrals are evaluated with Gauss–Legendre quadrature [41], and inter-element coupling is handled through the Harten–Lax–van Leer–Contact (HLLC) Riemann solver [51], which preserves sharp density interfaces. Time advancement is performed with a strong-stability-preserving third-order Runge–Kutta scheme (SSP-RK3) [52]. To suppress oscillations near shocks, a Krivodonova-type moment limiter [42] is employed in troubled cells identified by a modified TVB sensor. All simulations use a fixed CFL number of 0.1. This combination of high-order discretization, robust flux evaluation, and selective limiting provides accurate resolution of shock–interface interactions and vorticity dynamics essential for analyzing Mach number effects in light–heavy fluid layers.

4.2. Validation Against Benchmark Problems

To establish the accuracy and reliability of the present numerical simulations, three benchmark validation cases are considered. These cases involve direct comparison of the current results with well-documented experimental studies on shock-accelerated interfaces, thereby ensuring the fidelity of the solver in capturing both qualitative and quantitative aspects of instability evolution.

4.2.1. Shock-Accelerated Heavy V-Shaped Interface

The first validation case corresponds to the shock–interface interaction experiment of Luo et al. [53], where a planar shock of Mach number $M_s = 1.2$ impinges on a V-shaped air/SF_6 interface with an inclination angle of $\theta = 60^\circ$. Figure 2a presents a comparison of

Schlieren visualizations, demonstrating that the present simulations accurately reproduce the observed interface deformation, transmitted and reflected waves, and subsequent roll-up structures. Quantitative validation is provided in Figure 2b, where the temporal evolution of the upstream interface displacement, D_s, obtained from simulations, shows excellent agreement with experimental measurements.

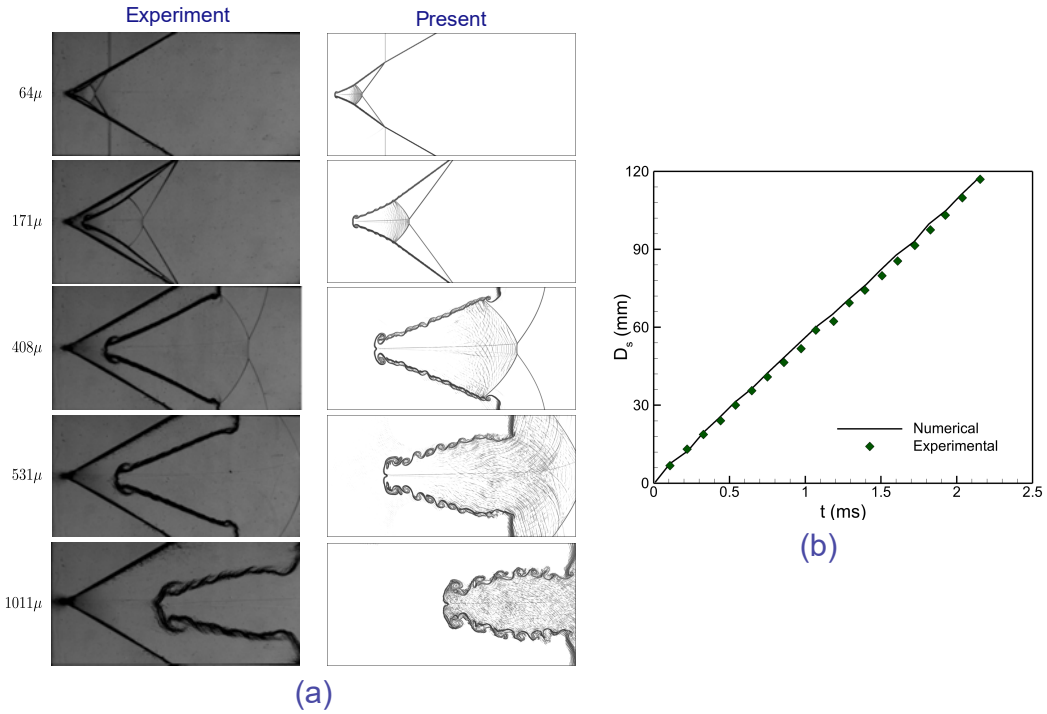

Figure 2. Comparison of (**a**) numerical Schlieren images and (**b**) the temporal evolution of the upstream interface displacement D_s between the experiment (reproduced with permission from [53], Cambridge University Press, 2016) and the present results for a shock-accelerated V-shaped air/SF_6 interface at $M_s = 1.2$.

4.2.2. Shock-Accelerated Heavy Elliptical Interface

The second benchmark focuses on the experiment by Ou and Zhai [54], in which a weak planar shock with Mach number $M_s = 1.24$ interacts with an initially oblate elliptical air/SF_6 bubble. Figure 3 compares the temporal sequence of Schlieren images from both the experiment and simulation. The numerical results capture the essential features of interface evolution, including the deformation of the elliptic bubble, its compression along the shock propagation direction, and the eventual development of small-scale roll-up at later times. The close agreement with experimental observations further confirms the robustness and predictive capability of the present DG solver.

4.2.3. Shock-Accelerated Light Cylindrical Interface

To further verify the accuracy of the present high-order DG solver, a classical benchmark case involving a shock-accelerated light cylindrical interface was examined. In this configuration, a planar shock wave with Mach number $M_s = 1.22$ impinges on a stationary helium cylinder immersed in nitrogen, a setup originally investigated experimentally by Haas and Sturtevant [25] and later simulated by Quirk and Karni [24]. This canonical problem provides a stringent validation of both shock-capturing accuracy and the solver's ability to reproduce complex interface deformation and vorticity generation.

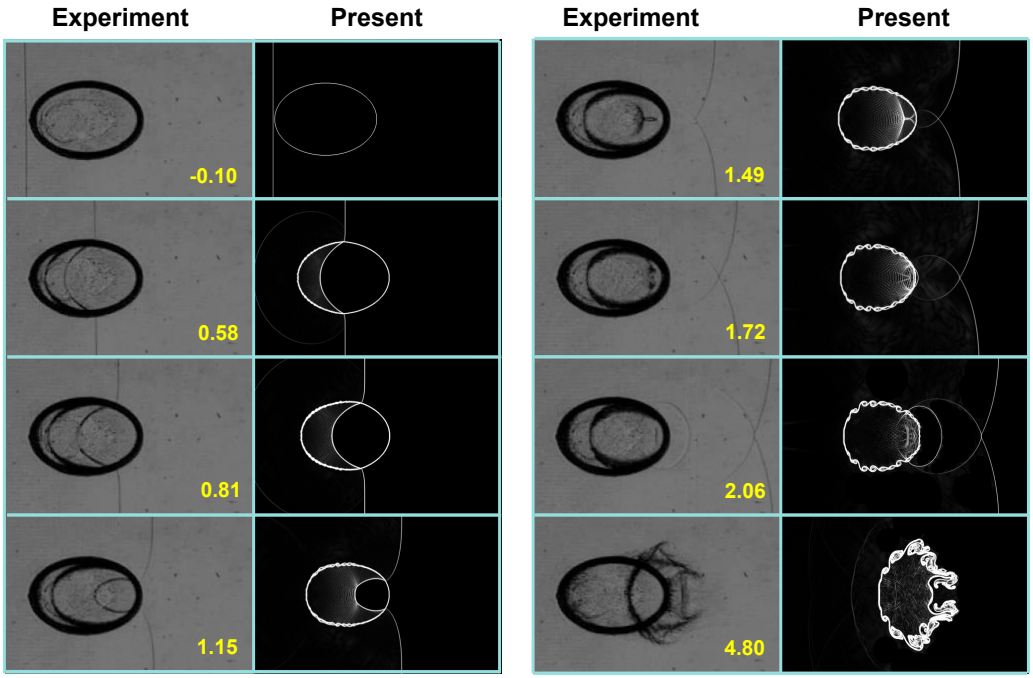

Figure 3. Comparison of numerical Schlieren images between the experimental two-dimensional results (reproduced with permission from [54], Springer Press, 2019) and the present numerical results for a shock-accelerated heavy elliptical interface with $M_s = 1.24$.

Figure 4 presents a qualitative comparison among the experimental Schlieren images, the previous computational results, and the present DG simulations at successive times of 32 μs, 62 μs, 82 μs, 102 μs, and 245 μs. The present results successfully replicate all major flow features observed in the reference studies, including the transmitted shock within the helium region, the reflected shock in the ambient gas, and the development of a curved contact interface subjected to baroclinic vorticity deposition. The early frames capture the initial compression and refraction of the shock at the interface, while the intermediate stages clearly show the formation of a counter-rotating vortex pair and the onset of roll-up due to the KHI. At late times, the interface exhibits pronounced elongation, jet formation, and secondary wave interactions, demonstrating the solver's ability to sustain physically realistic morphology and small-scale structures.

Quantitative validation is provided in Figure 5, which compares the temporal evolution of characteristic interface points—the upstream interface (UI), downstream interface (DI), and jet tip—between the experimental data of Haas and Sturtevant [25] and the present simulations. The trajectories of these points exhibit nearly identical slopes and curvature, confirming that the present solver accurately reproduces interface acceleration, deformation rate, and jet penetration distance. This level of agreement attests to the solver's ability to capture not only the global interface motion but also localized jet dynamics that are sensitive to vorticity deposition. Further verification is offered in Figure 6, which compares the temporal variation of the circulation magnitude between the results of Quirk and Karni [24] and the present computations. The close correspondence in circulation growth indicates that the DG framework precisely captures the baroclinic vorticity generation mechanism and its temporal evolution following shock impact. The quantitative agreement across multiple diagnostics—interface trajectories and circulation—establishes that the present solver reproduces both the kinematic and dynamic aspects of the canonical shock–helium cylinder interaction.

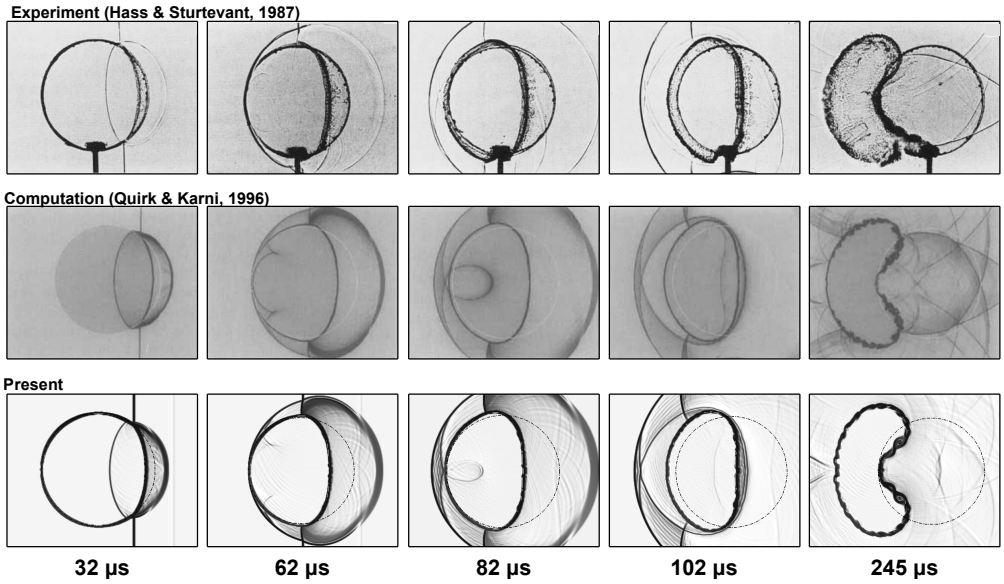

Figure 4. Comparison of numerical Schlieren images between the experimental results (reproduced with permission from [25], Cambridge University Press, 1987), computational results (reproduced with permission from [24], Cambridge University Press, 1996), and the present numerical results for a shock-accelerated light cylindrical interface with $M_s = 1.22$.

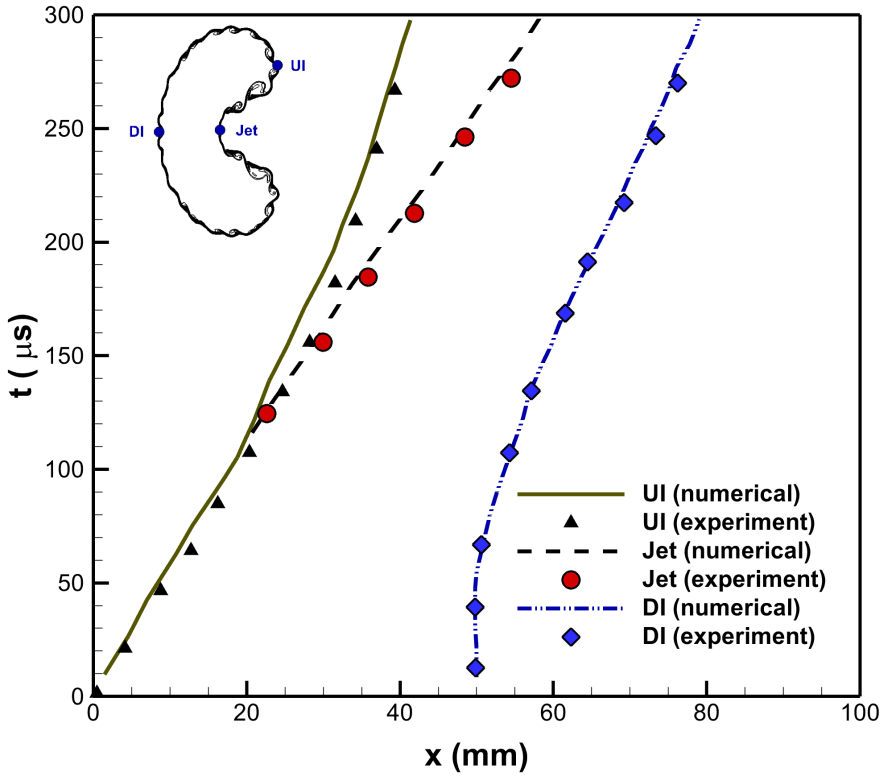

Figure 5. Quantitative comparison of characteristic interface locations between the experimental results (reproduced with permission from [25], Cambridge University Press, 1987) and the present numerical results for a shock-accelerated light cylindrical interface with $M_s = 1.22$. The tracked points include the upstream interface (UI), downstream interface (DI), and jet tip, as indicated in the inset schematic.

Notably, Wang et al. [44,45] reported high-resolution experiments on shock–vortex and shock-train interactions in compressible flows, highlighting vorticity amplification and the formation of small-scale coherent structures. The present simulations reproduce similar early-stage features, where baroclinic torque drives localized vorticity generation

and interface deformation. This agreement with experimental observations validates the accuracy of the high-order DG framework and supports its reliability in analyzing shock-driven interfacial instabilities.

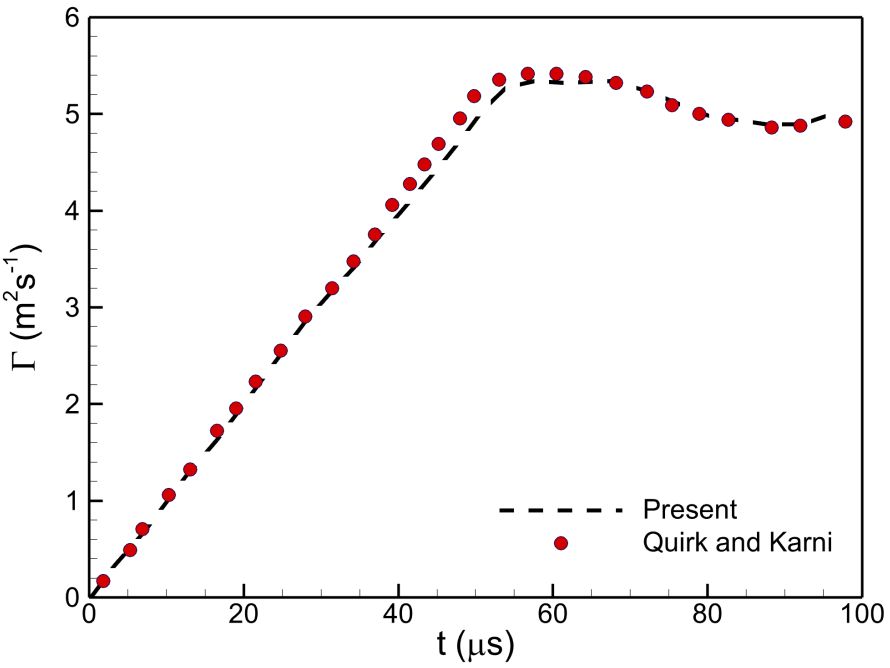

Figure 6. Comparison of circulation magnitude between the computational results (reproduced with permission from [24], Cambridge University Press, 1996) and the present numerical results for a shock-accelerated light cylindrical interface with $M_s = 1.22$.

4.3. Grid Resolution Strategy

To ensure the numerical accuracy and stability of the present simulations, a systematic grid-resolution study was carried out for the shock-accelerated single-mode light–heavy fluid layer with $M_s = 1.25$. The temporal evolution of the flow field was compared across three uniform Cartesian grids: Grid–I (400 × 200), Grid–II (800 × 400), and Grid–III (1200 × 600). The non-dimensional time parameter was defined as

$$\tau = \frac{t}{t_0} = \frac{tV_i}{L}. \tag{13}$$

where V_i is the incident shock velocity and L is the characteristic wavelength of the interface perturbation.

Figure 7 presents the instantaneous density contours at $\tau = 20$ for the three grid levels. On the coarse grid (Grid–I), the density gradients near the interface are noticeably diffused, leading to smearing of the contact surface and an underprediction of small-scale roll-up structures. Refinement to Grid–II provides sharper resolution of the shock front and the transmitted and reflected waves, and it also captures the primary vortex pair induced by baroclinic torque. Further refinement to Grid–III results in enhanced definition of secondary vortices and a more distinct interface morphology; however, the global flow features remain nearly identical to those obtained with Grid–II, indicating numerical convergence of the solution. This trend is confirmed quantitatively in Figure 8, which compares density profiles along the centerline ($y = 50$ mm) at $\tau = 20$. The coarse grid substantially underestimates the density gradients across the interface, whereas the results from Grid–II and Grid–III nearly overlap. Minor discrepancies confined to the vicinity of the interface suggest that the medium grid adequately resolves all essential features.

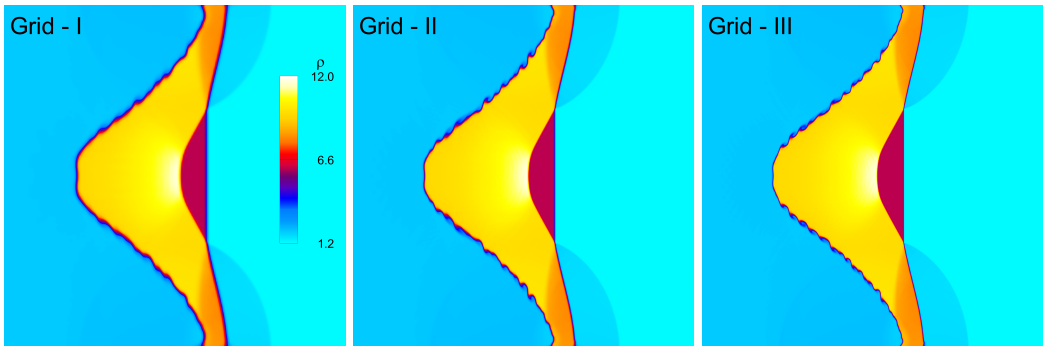

Figure 7. Density contours at nondimensional time $\tau = 20$ for a shock-accelerated single-mode light–heavy fluid layer, computed on three different grids: Grid–I (400 × 200), Grid–II (800 × 400), and Grid–III (1200 × 600).

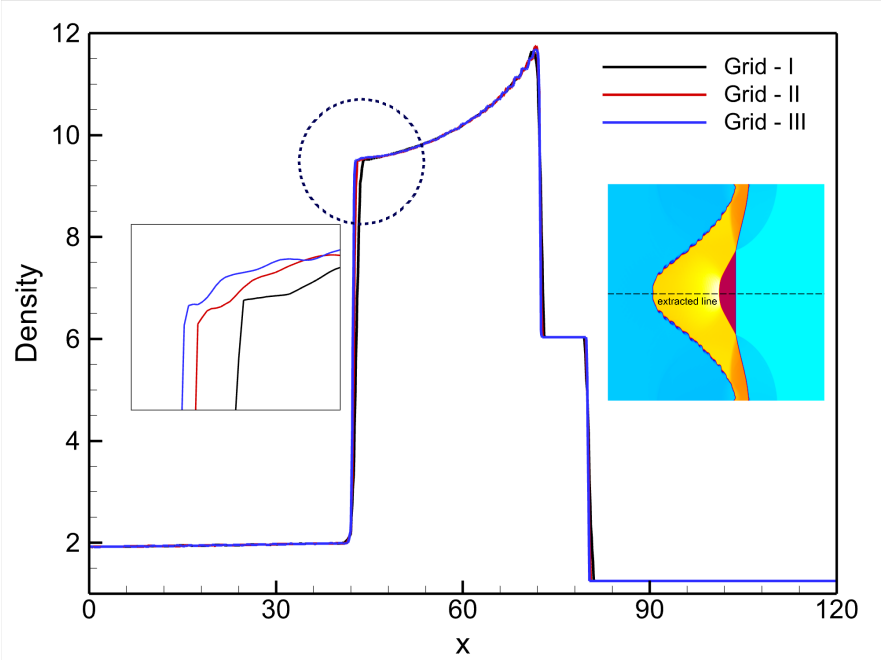

Figure 8. Density profiles along the centerline ($y = 50$ mm) at $\tau = 20$ for a shock-accelerated single-mode light–heavy fluid layer, computed on three different grids: Grid–I (400 × 200), Grid–II (800 × 400), and Grid–III (1200 × 600).

Figure 9 illustrates the temporal evolution of two key diagnostic quantities—the baroclinic vorticity magnitude $|\omega_{\text{bar}}|$ and the enstrophy Ω—for the single-mode light–heavy fluid layer subjected to a shock of $M_s = 1.25$, computed on three grid resolutions. Both quantities exhibit an initial sharp increase immediately after shock impact due to impulsive vorticity deposition at the perturbed interface, followed by gradual growth associated with vortex roll-up and secondary interactions. As the grid is refined from 400 × 200 (Grid–I) to 800 × 400 (Grid–II), the magnitudes of $|\omega_{\text{bar}}|$ and Ω increase substantially, indicating improved resolution of small-scale shear layers and enhanced capture of baroclinic torque effects. Further refinement to 1200 × 600 (Grid–III) yields quantitatively higher values but exhibits similar temporal trends to Grid–II, suggesting that the principal flow dynamics are well resolved. The convergence of both diagnostic curves at later times confirms that the numerical solution becomes grid-independent beyond the medium resolution. Consequently, the 1200 × 600 grid was selected for production simulations to ensure accurate yet computationally efficient modeling of vorticity generation and instability growth.

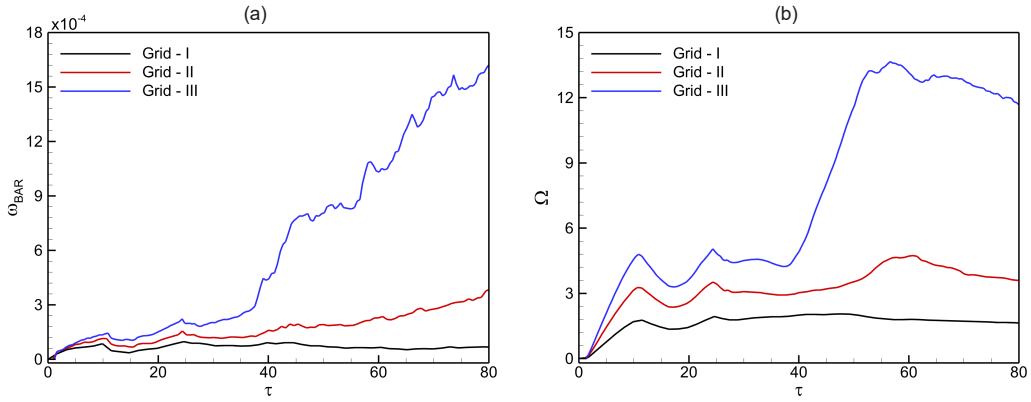

Figure 9. Temporal evolution of diagnostic quantities for a shock-driven single-mode light–heavy fluid layer with $M_s = 1.25$, using three different grids: (**a**) baroclinic vorticity magnitude $|\omega_{\text{bar}}|$, and (**b**) enstrophy Ω.

5. Results and Discussion

In this section, the numerical results are analyzed to elucidate the effect of shock Mach number on instability evolution at the light–heavy fluid layer. The discussion combines qualitative flow-field visualizations with quantitative diagnostics to highlight how variations in shock strength influence vorticity generation, interface morphology, and mixing dynamics.

5.1. Flow Field Evolution

Figures 10–12 present the temporal evolution of density contours and Schlieren images for shock-accelerated instabilities at a single-mode light–heavy fluid layer across a range of incident Mach numbers. A clear progression is observed, where increasing shock strength systematically modifies vorticity deposition, interface deformation, and the transition from linear to nonlinear instability growth.

For the weakest shock case ($M_s = 1.15$, as illustrated in Figure 10a), the incident shock (IS) interacts with the perturbed upstream interface, producing a reflected shock (RS) in the ambient region and a transmitted shock (TS1) inside the heavy layer. The misalignment of pressure and density gradients generates baroclinic vorticity, but its magnitude is relatively small, leading to the slow growth of bulges and spikes. As the transmitted shock reaches the downstream interface (DS), additional transmitted (TS2) and reflected (RTS) waves are formed, though the interface deformation remains limited. At later times ($\tau \geq 50$), KH instabilities appear, but the roll-ups are weak and the jet penetration is subdued, producing a relatively broad interface morphology. When the Mach number increases slightly ($M_s = 1.25$, as shown in Figure 10b), the baroclinic torque strengthens, resulting in larger circulation deposition along the interface. The transmitted shock traverses the heavy layer more rapidly, enhancing secondary wave interactions at the downstream interface. Consequently, KH instabilities emerge earlier, spikes sharpen, and bubbles thin compared to the $M_s = 1.15$ case. By later times, a more distinct jet develops, signaling the onset of stronger instability growth and mixing.

At the intermediate Mach number ($M_s = 1.50$, as illustrated in Figure 11), the instability enters a vigorous nonlinear stage. Early shock-interface misalignment generates stronger circulation, and by $\tau = 25$–35, the interface develops pronounced KH roll-ups and fine-scale eddies. These vortical structures amplify deformation, rolling up the heavy fluid into the light medium. At later times, sharp spikes penetrate deeply, bubbles rise prominently, and a distinct jet emerges. Compared to the lower Mach number cases, $M_s = 1.50$ exhibits much earlier KH onset and more complex interface morphology with thinner spikes and stronger jet-like structures.

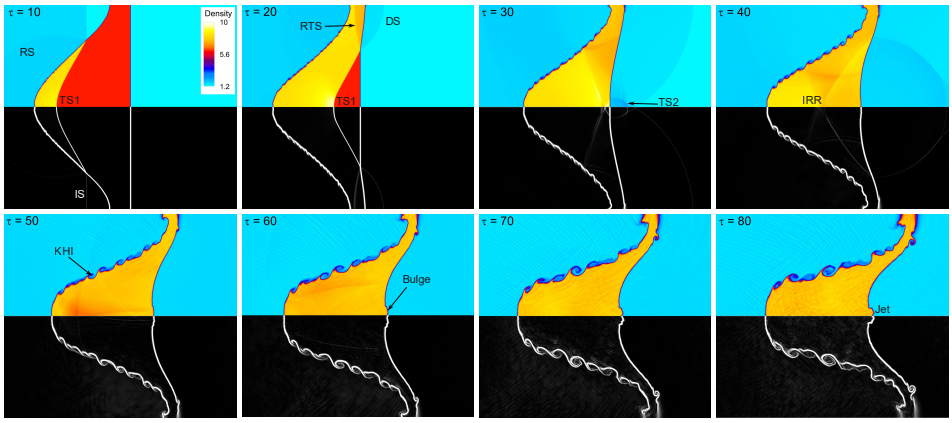

(a) M_s = 1.15

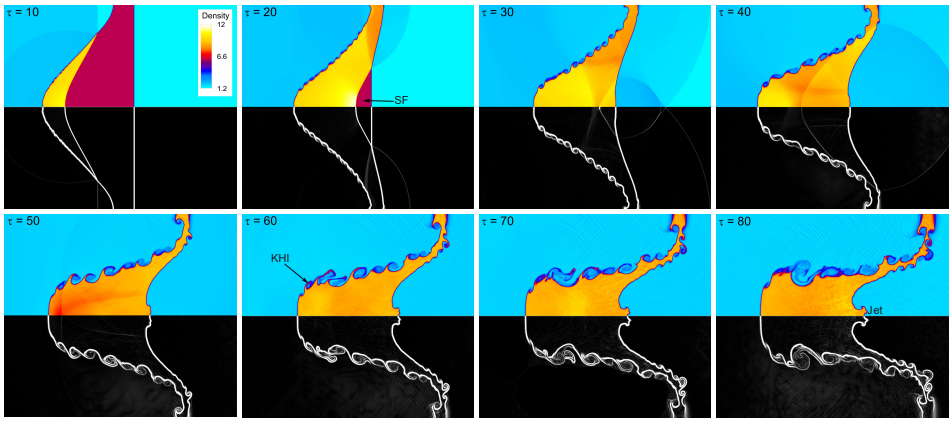

(b) M_s = 1.25

Figure 10. Temporal evolution of density contours (upper half) and corresponding Schlieren visualizations (lower half) for a shock-accelerated light–heavy fluid layer at incident Mach numbers (**a**) $M_s = 1.15$ and (**b**) $M_s = 1.25$. The images show the incident shock (IS), reflected shock (RS), transmitted shocks (TS1, TS2), shock focusing (SF), and reflected–transmitted waves (RTS). Enhanced baroclinic vorticity deposition and early Kelvin–Helmholtz (KH) roll-ups are visible at higher M_s values, indicating stronger interface deformation and jet penetration.

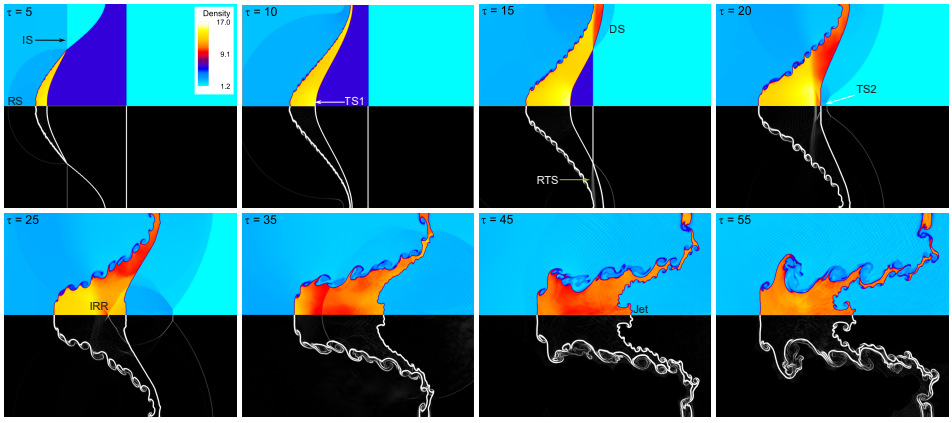

Figure 11. Temporal evolution of density contours (upper half) and Schlieren visualizations (lower half) for a shock-accelerated light–heavy fluid layer at an incident Mach number of $M_s = 1.50$. The images show the successive interaction of the incident shock (IS) with the perturbed upstream interface, the formation of the reflected shock (RS), transmitted shocks (TS1, TS2), and reflected–transmitted waves (RTS). The misalignment of pressure and density gradients leads to strong baroclinic vorticity deposition, resulting in early Kelvin–Helmholtz (KH) roll-ups, spike sharpening, and jet formation.

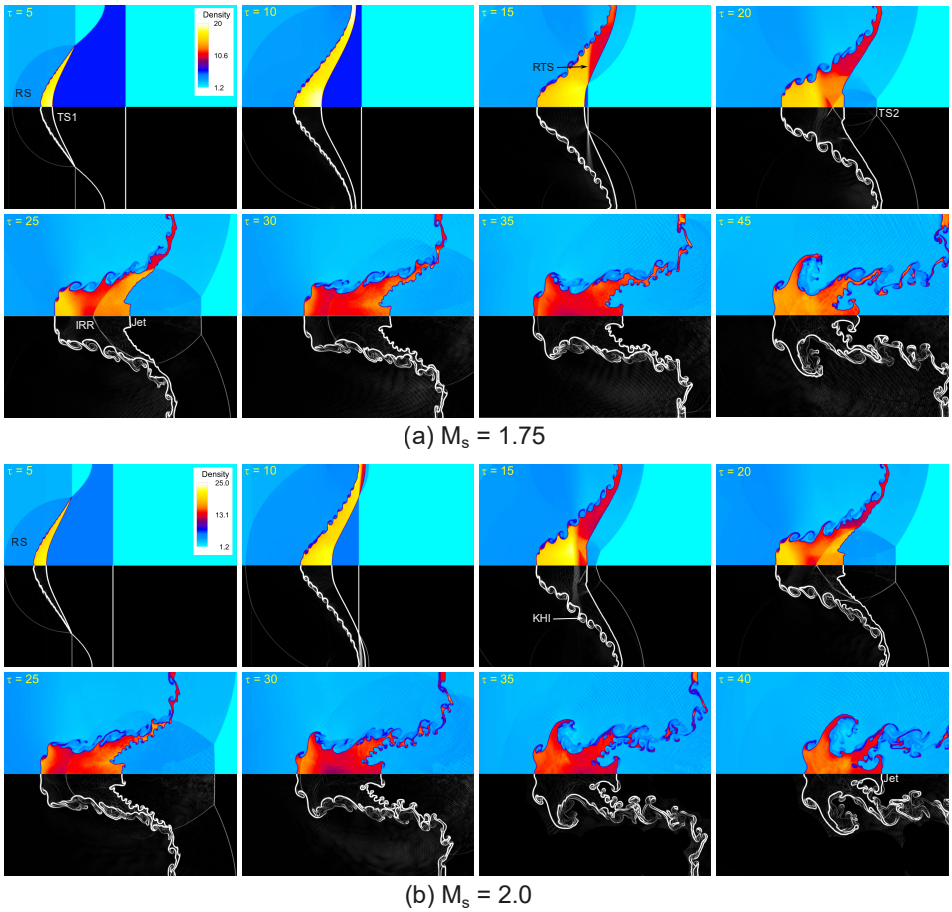

Figure 12. Temporal evolution of density contours (upper half) and Schlieren images (lower half) for a shock-accelerated light–heavy fluid layer at (**a**) $M_s = 1.75$ and (**b**) $M_s = 2.0$. The incident shock (IS) interacts with the perturbed interface, producing reflected (RS) and transmitted shocks (TS1, TS2) and reflected–transmitted waves (RTS). Strong shock focusing (SF) and baroclinic vorticity deposition lead to early Kelvin–Helmholtz (KH) roll-ups, jet formation, and small-scale fragmentation, illustrating the transition to highly nonlinear instability growth.

At higher Mach numbers ($M_s = 1.75$ and $M_s = 2.00$, as displayed in Figure 12), the instability evolves violently and transitions quickly into the nonlinear regime. For $M_s = 1.75$, enhanced baroclinic vorticity and strong downstream interactions lead to rapid roll-up, elongated bubble structures, and the formation of a prominent jet accompanied by secondary eddies. At the highest Mach number studied ($M_s = 2.00$), the shock–interface interaction produces very strong vorticity deposition and extremely early KH onset ($\tau \leq 20$). The interface undergoes severe distortion, with sharp spike thinning, vortex pairing, and small-scale fragmentation dominating the dynamics. By later times ($\tau \geq 35$), multiple jets and highly convoluted vortical structures appear, representing the most intense instability growth among all cases. In summary, the comparative analysis across Figures 10–12 demonstrates that increasing Mach number progressively amplifies baroclinic vorticity generation, accelerates the onset of KH instabilities, sharpens interface structures, and enhances jet penetration. These effects drive a continuous transition from weak, quasi-linear growth at low Mach numbers to a strongly nonlinear, multi-scale vortical regime at the strongest shock strengths.

Building on the flow-field observations presented in Figures 10–12, we extend our investigation by examining the temporal evolution of interface deformation across a broader range of Mach numbers. This further analysis highlights how increasing shock strength systematically alters perturbation growth, spike–bubble dynamics, and interface morphology.

Figure 13 illustrates the temporal evolution of interface deformation for shock-accelerated single-mode light–heavy fluid layers subjected to a sequence of incident Mach numbers ranging from $M_s = 1.15$ to $M_s = 2.00$. The overlaid contours at successive nondimensional times τ provide a direct comparison of how shock strength influences the growth rate, morphology, and complexity of the interface. For the weakest shocks ($M_s = 1.15$ and $M_s = 1.25$; Figure 13a,b), interface growth is relatively slow, with broad bulges and shallow spikes dominating the early-to-intermediate stages. The KH instabilities appear only at later times, producing limited roll-up and subdued jet penetration. The interface retains a smooth structure for extended periods, reflecting weaker baroclinic vorticity deposition. At the intermediate Mach number ($M_s = 1.50$; Figure 13c), instability growth accelerates significantly. Earlier onset of KH instabilities produces visible roll-ups, finer interface undulations, and increased spike sharpening. By later times, the interface displays enhanced asymmetry between spikes and bubbles, together with a distinct jet, indicating a stronger nonlinear response compared with the lower Mach number cases. For stronger shocks ($M_s = 1.75$ and $M_s = 2.00$; Figure 13d,e), the interface undergoes rapid and violent deformation. The higher baroclinic torque amplifies circulation, leading to early KH roll-ups, sharp spike penetration, and strong bubble elongation. At $M_s = 1.75$, vortex pairing and secondary eddies dominate the interface, while at $M_s = 2.00$ the deformation becomes highly irregular and multi-scale, with multiple jets, fine-scale fragmentation, and a fully convoluted interface.

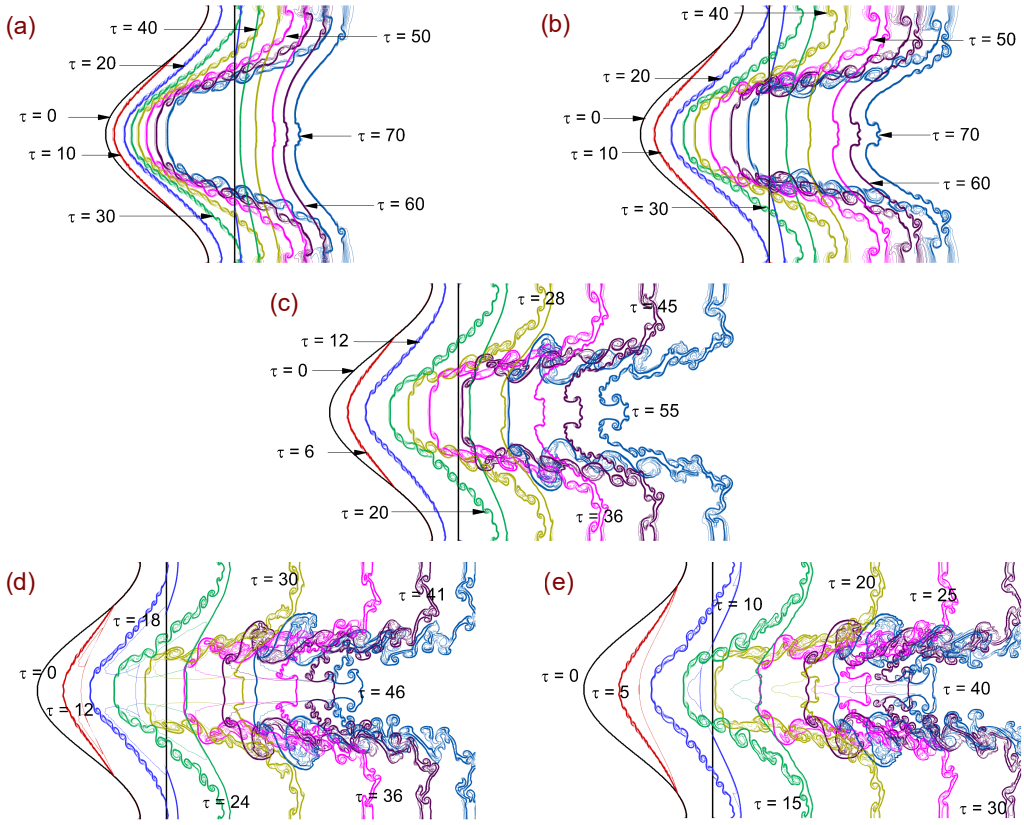

Figure 13. Temporal evolution of interface deformation for shock-accelerated single-mode light–heavy fluid layers at different Mach numbers: (**a**) $M_s = 1.15$, (**b**) $M_s = 1.25$, (**c**) $M_s = 1.5$, (**d**) $M_s = 1.75$, and (**e**) $M_s = 2.0$.

5.2. Shock Focusing and Pressure Distribution

Figure 14 illustrates the temporal evolution of pressure contours for shock-accelerated single-mode light–heavy fluid layers over a Mach number range of $M_s = 1.15$–2.00. The results emphasize the influence of shock focusing (SF) and high-pressure zones (HPZ) on

instability amplification. For the weak shock case ($M_s = 1.15$), the incident wave partially reflects and transmits through the heavy layer, generating mild SF near the perturbed interface. The pressure field remains smooth with weak localized compression, and HPZ formation is minimal, consistent with the delayed onset of nonlinear deformation. At $M_s = 1.25$, shock convergence near the sinusoidal troughs strengthens SF and produces distinct HPZs adjacent to the interface. The enhanced pressure gradients increase baroclinic torque, promoting stronger spike–bubble growth compared with the weaker case. At the intermediate strength ($M_s = 1.50$), SF becomes more pronounced, producing intense compression at the interface bulges. The HPZs act as localized accelerators for KH roll-ups and asymmetric spike–bubble development. For higher Mach numbers ($M_s = 1.75$ and $M_s = 2.00$), SF effects dominate. Multiple focusing regions appear simultaneously, producing sharp HPZs and irregular pressure distributions. These concentrated compression zones amplify vorticity deposition, sharpen spikes, and induce early KH instabilities. At the highest Mach number ($M_s = 2.00$), strong coupling between SF and HPZ formation leads to complex jet structures and small-scale fragmentation, illustrating how shock focusing drives instability intensification and parallels the behavior observed in confined shock-train systems [45].

Figure 15 shows the temporal evolution of pressure distribution along the centerline ($y = 50$ mm) for shock-accelerated single-mode light–heavy fluid layers at different Mach numbers. These distributions provide quantitative insight into how pressure loading evolves with time and how increasing Mach number modifies compression, focusing, and instability growth. For the lowest Mach number ($M_s = 1.15$; Figure 14a), the pressure profiles remain relatively smooth, with only moderate increases across the interface region. Localized compression is weak, consistent with limited baroclinic deposition and delayed nonlinear interface deformation observed in earlier figures. At slightly higher Mach number ($M_s = 1.25$; Figure 14b), stronger pressure gradients appear near the interface as transmitted and reflected shocks interact with the heavy layer. This produces more pronounced local peaks in the pressure distribution, correlating with enhanced circulation and earlier onset of KH instabilities. In the intermediate case ($M_s = 1.50$; Figure 11c), pressure focusing effects become more evident. The profiles show sharper gradients and higher peaks, reflecting the formation of high-pressure zones (HPZs) at the interface. These elevated pressures accelerate instability growth, sharpening spikes and promoting asymmetric bubble–spike development. At higher Mach numbers ($M_s = 1.75$ and $M_s = 2.00$; Figure 14d,e), the pressure field becomes highly nonuniform. Strong localized peaks emerge as shock focusing (SF) intensifies, and the HPZ regions expand. Particularly for $M_s = 2.00$, the profiles display sharp discontinuities and strong compression zones, consistent with the violent interface deformation, multiple jet formation, and strongly nonlinear, multi-scale vortical features observed in previous figures.

5.3. Dynamics of Vorticity Generation

Figure 16 schematically illustrates the vorticity generation mechanism in a shock-accelerated single-mode light–heavy fluid layer. Prior to shock impact, the pressure (∇p) and density ($\nabla \rho$) gradients are aligned, yielding zero baroclinic torque. Upon interaction with the perturbed interface, the incident shock induces local misalignment between ∇p and $\nabla \rho$, particularly near the interface peaks and troughs, generating a vorticity sheet along the interface. This deposited vorticity initiates spike–bubble growth and evolves into vortical structures through shear-induced roll-up. During the post-shock phase, these vortices intensify KH instabilities, enhancing interfacial mixing. The schematic emphasizes baroclinic torque as the dominant mechanism governing instability evolution and transition to nonlinear dynamics. Moreover, it connects with recent advances in active vortex control,

where controlled vorticity deposition—such as via shock–vortex interactions or plasma-assisted actuation—has been shown to modulate interface roll-up and mixing intensity [47].

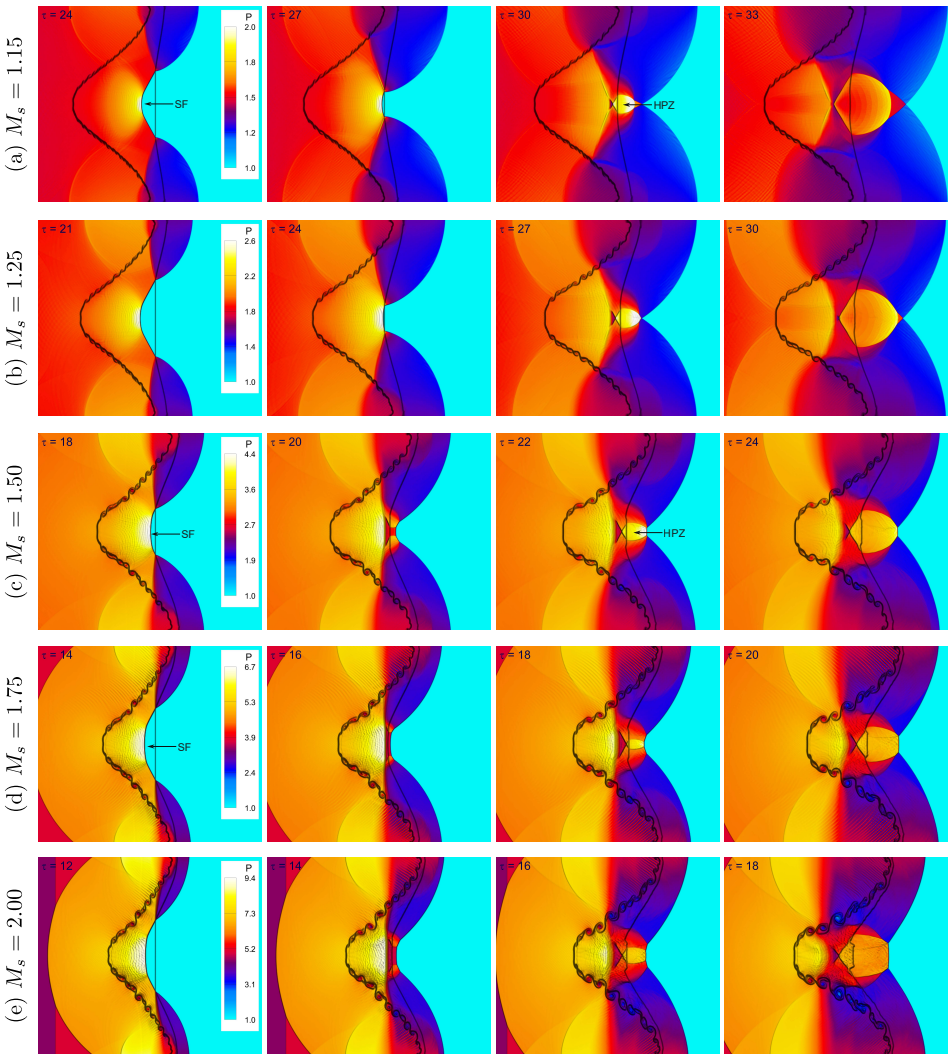

Figure 14. Temporal evolution of pressure contours for shock-accelerated single-mode light–heavy fluid layers at different Mach numbers: (**a**) $M_s = 1.15$, (**b**) $M_s = 1.25$, (**c**) $M_s = 1.5$, (**d**) $M_s = 1.75$, and (**e**) $M_s = 2.0$.

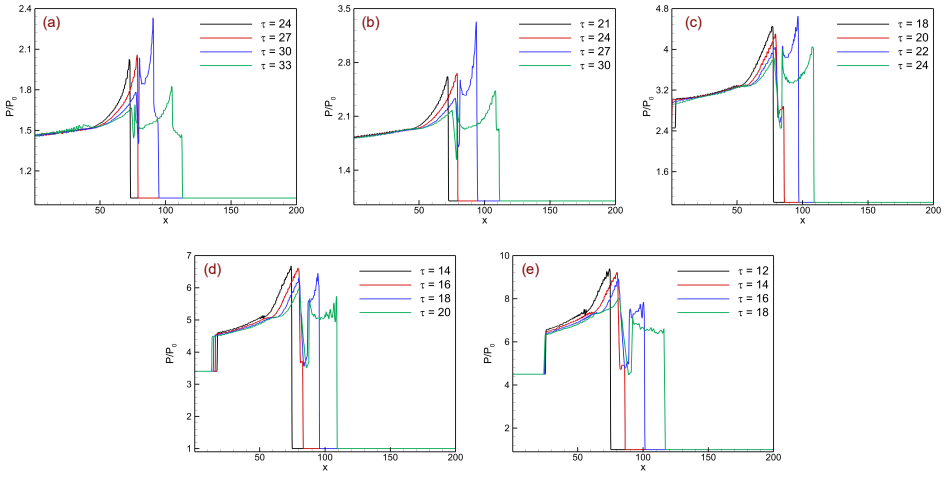

Figure 15. Temporal evolution of pressure distribution along the centerline ($y = 50$ mm) for a shock-accelerated single-mode light–heavy fluid layer at different Mach numbers: (**a**) $M_s = 1.15$, (**b**) $M_s = 1.25$, (**c**) $M_s = 1.5$, (**d**) $M_s = 1.75$, and (**e**) $M_s = 2.0$.

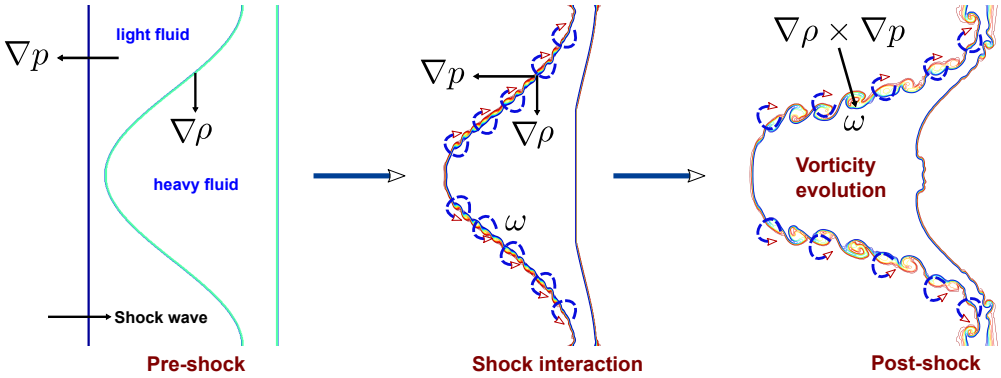

Figure 16. Schematic illustration of vorticity generation in a shock-accelerated single-mode light–heavy fluid layer. The sequence highlights (i) the pre-shock state, (ii) shock–interface interaction leading to the misalignment of pressure and density gradients ($\nabla \rho \times \nabla p$), and (iii) the subsequent baroclinic vorticity deposition and the evolution of vortical structures along the perturbed interface.

Figure 17 illustrates the temporal evolution of vorticity distribution in shock-accelerated single-mode light–heavy fluid layers at different incident Mach numbers ($M_s = 1.15$–2.00). The vorticity fields provide direct evidence of baroclinic deposition during shock–interface interaction and the subsequent development of vortical structures that drive interface deformation and mixing. For the weak shock case ($M_s = 1.15$), vorticity is deposited primarily along the interface immediately after shock passage, with relatively low intensity and limited roll-up. The resulting structures remain smooth and elongated, leading to gradual spike and bubble development. At a slightly higher Mach number ($M_s = 1.25$), stronger baroclinic torque produces more pronounced vorticity layers on both sides of the interface. These layers begin to roll up earlier, forming coherent vortical structures that enhance interface asymmetry and promote moderate mixing. For the intermediate case ($M_s = 1.50$), vorticity amplification is more substantial. The deposition becomes highly asymmetric, with stronger vortical patches forming near the spike tips and bubble shoulders. The KH roll-ups are clearly observed, which significantly accelerate the transition from linear perturbation growth to nonlinear deformation. At higher Mach numbers ($M_s = 1.75$ and $M_s = 2.00$), the vorticity distribution becomes increasingly complex and fragmented. Stronger baroclinic generation leads to the formation of multiple vortical structures, vortex pairing, and fine-scale breakdown along the interface. For $M_s = 2.00$, small-scale eddies dominate the field, indicating enhanced interface deformation and complex multi-scale vortical interactions.

5.4. Quantitative Diagnostics

To extend our investigation, we now examine the spatially integrated contributions of vorticity production mechanisms, as described by the vorticity transport equation for compressible inviscid flows (Equation (12)). In the context of shock–interface interactions, two principal source terms govern vorticity evolution: the dilatational contribution, $-\omega(\nabla \cdot \mathbf{u})$, and the baroclinic torque, $\frac{1}{\rho^2}\nabla \rho \times \nabla p$. The dilatational term accounts for compressibility effects linked to local expansion and compression of fluid elements, whereas the baroclinic term arises from the misalignment of pressure and density gradients and constitutes the dominant source of vorticity generation in RMI.

To quantify the temporal evolution of these contributions, we define spatially integrated measures over the computational domain D:

$$\omega_{DIL}(t) = \int_D \left| -\omega(\nabla \cdot \mathbf{u}) \right| dx\, dy, \tag{14}$$

$$\omega_{BAR}(t) = \int_D \left| \frac{1}{\rho^2} \nabla\rho \times \nabla p \right| dx\, dy, \tag{15}$$

where $\omega_{DIL}(t)$ and $\omega_{BAR}(t)$ represent the global strength of the dilatational and baroclinic contributions, respectively. These integrated quantities allow us to directly compare the relative importance of compressibility-driven and baroclinic mechanisms in the evolution of shock-accelerated interfaces.

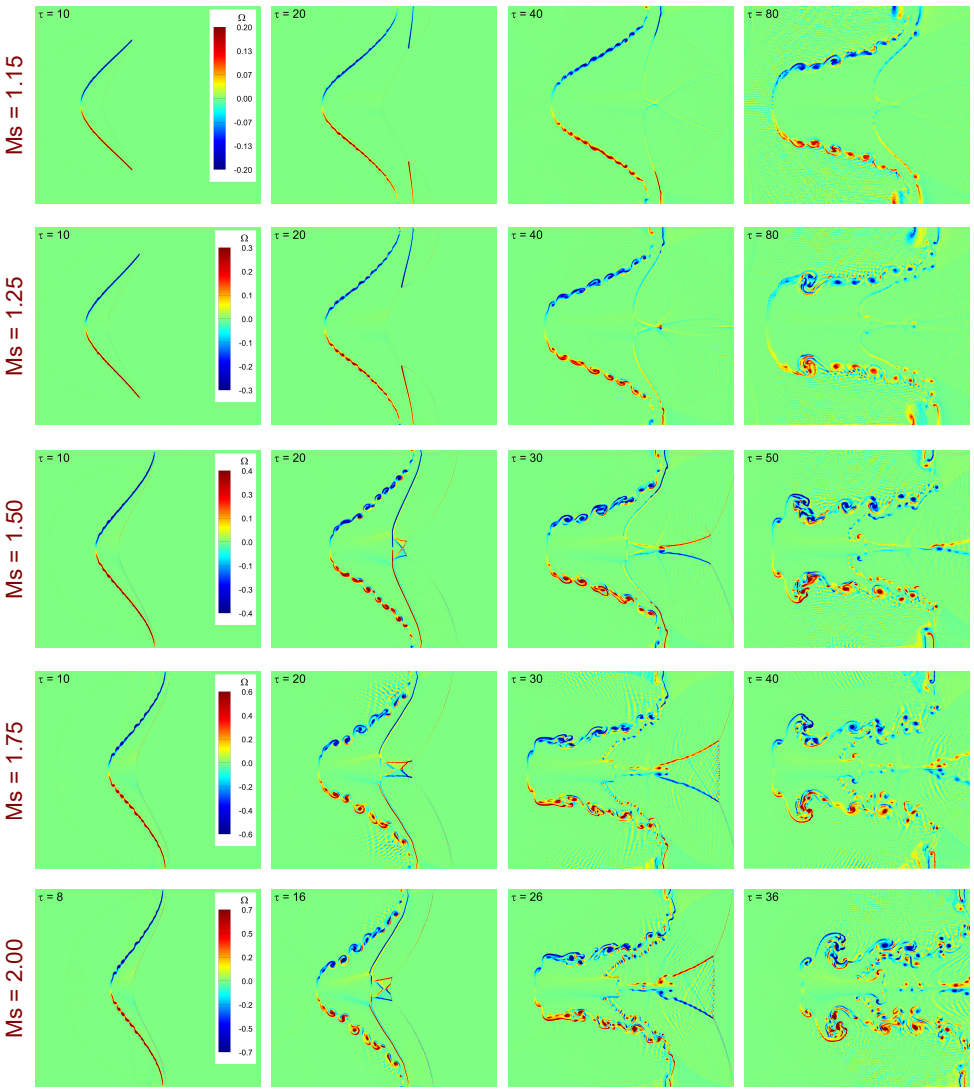

Figure 17. Temporal evolution of vorticity distribution in shock-accelerated single-mode light–heavy fluid layers at different Mach numbers: $M_s = 1.15, 1.25, 1.50, 1.75, 2.00$.

Figure 18 presents the temporal evolution of the spatially integrated vorticity production terms in shock-accelerated light–heavy fluid layers at different Mach numbers. The dilatational contribution, ω_{DIL}, in Figure 18a quantifies vorticity induced by local expansion and compression, while the baroclinic term, ω_{BAR}, in Figure 18b arises from the misalignment between pressure and density gradients.

At low Mach numbers ($M_s = 1.15$–1.25), both contributions remain weak, consistent with limited interface deformation and delayed secondary instability. As M_s increases to 1.50, both terms amplify, with ω_{BAR} dominating and driving coherent vortex roll-ups, while ω_{DIL} responds more strongly to intensified compression fields. At higher Mach numbers ($M_s = 1.75$–2.00), rapid amplification of both components occurs; ω_{BAR} attains the highest magnitude, confirming its primary role in vorticity generation, whereas ω_{DIL} becomes increasingly significant in modulating small-scale flow structures. The results in Figure 18

reveal that, although baroclinic torque remains the dominant source of vorticity generation across all Mach numbers, the relative contribution of dilatational effects increases markedly at higher Mach numbers ($M_s \geq 1.5$). This trend arises from enhanced flow compressibility and strong local pressure focusing near sinusoidal troughs, which create alternating regions of expansion and compression. The associated dilatational term, $-\omega(\nabla \cdot \mathbf{u})$, serves as a secondary amplification mechanism that intensifies existing vortices and promotes small-scale fragmentation. Thus, while baroclinic torque initiates the primary circulation, compressibility-induced dilatation accelerates the redistribution of vorticity, leading to an earlier transition into the nonlinear regime.

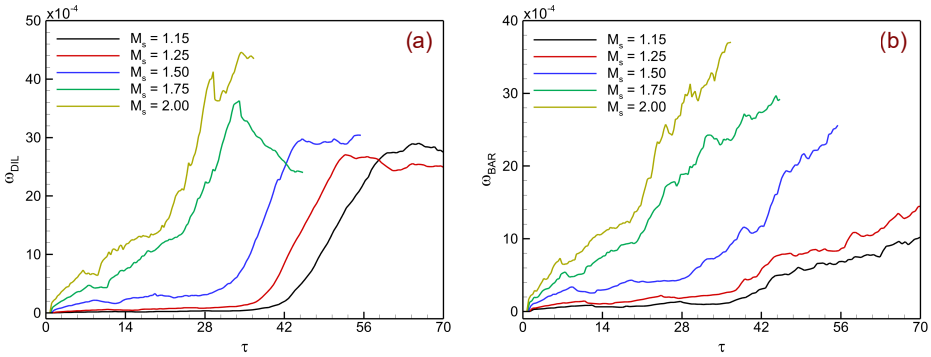

Figure 18. Temporal evolution of spatially integrated vorticity production terms in shock-accelerated single-mode light–heavy fluid layers at different Mach numbers: (**a**) dilatational contribution (ω_{DIL}) associated with compressibility effects, and (**b**) baroclinic contribution (ω_{BAR}) arising from misaligned pressure and density gradients.

To further characterize the intensity of vortical structures generated during the shock-driven instability, we analyze the temporal evolution of the maximum and minimum vorticity within the computational domain. These extrema provide a direct measure of the circulation strength deposited along the perturbed interface and capture the subsequent development of roll-ups and fine-scale vortices. The extrema are defined as

$$\omega_{\max}(t) = \max_{\mathbf{x}\in D} \omega(\mathbf{x}, t), \qquad \omega_{\min}(t) = \min_{\mathbf{x}\in D} \omega(\mathbf{x}, t), \tag{16}$$

where $\omega(\mathbf{x}, t) = (\nabla \times \mathbf{u})(\mathbf{x}, t)$ is the scalar vorticity field in two dimensions and D denotes the computational domain. In the discrete numerical framework, these quantities are evaluated at each time step as

$$\omega_{\max}(t^n) = \max_{i,j} \omega_{i,j}(t^n), \qquad \omega_{\min}(t^n) = \min_{i,j} \omega_{i,j}(t^n). \tag{17}$$

Tracking $\omega_{\max}(t)$ and $\omega_{\min}(t)$ enables us to quantify the asymmetry between counter-rotating vortical regions and to assess how increasing Mach number enhances baroclinic circulation, thereby accelerating the transition from the linear growth regime to nonlinear roll-ups and mixing dynamics.

Figure 19 presents the temporal evolution of vorticity extrema for shock-accelerated single-mode light–heavy fluid layers at different Mach numbers. Figure 19a shows the maximum vorticity, $\omega_{\max}$, while Figure 19b shows the minimum vorticity, $\omega_{\min}$. These diagnostics provide direct insight into the strength of circulation deposited at the perturbed interface and reveal the asymmetry between clockwise and counterclockwise vortical regions as the instability evolves. For the weakest shock case ($M_s = 1.15$), both $\omega_{\max}$ and $\omega_{\min}$ remain small in magnitude throughout the simulation. The extrema exhibit a gradual rise followed by saturation at modest levels, consistent with weak baroclinic deposition and the slow development of interface roll-ups. At $M_s = 1.25$, the extrema grow more strongly.

ω_{max} increases steadily and reaches a higher peak, while ω_{min} drops to more negative values, indicating stronger counter-rotating vortical structures. This reflects enhanced circulation deposition and the earlier onset of KH instabilities compared with the lower Mach number case. For the intermediate shock strength ($M_s = 1.50$), both extrema amplify rapidly. Distinct peaks in ω_{max} correspond to vigorous roll-up of the interface, while ω_{min} reaches large negative magnitudes due to the deep penetration of heavy-fluid spikes. These results highlight the nonlinear growth regime, where vortical structures intensify and secondary instabilities contribute to mixing. At higher Mach numbers ($M_s = 1.75$ and $M_s = 2.00$), the vorticity extrema exhibit the strongest amplification and the most unsteady behavior. Large oscillations in ω_{max} reflect the repeated roll-up and breakup of vortical structures, while ω_{min} attains sustained large negative values, confirming strong asymmetry in circulation.

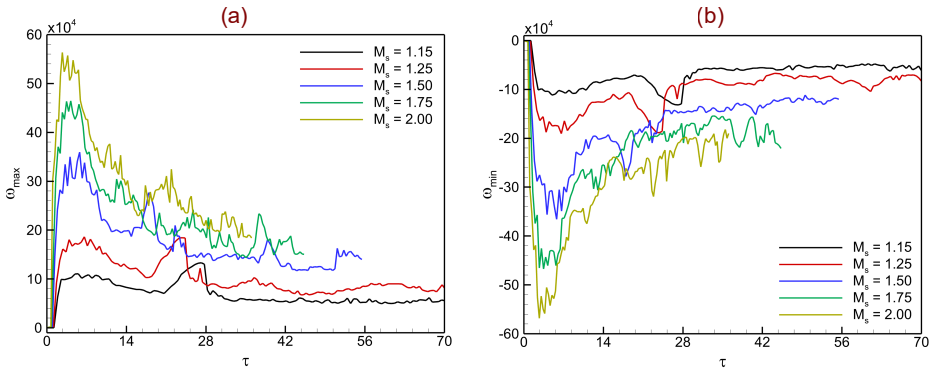

Figure 19. Temporal evolution of vorticity extrema in shock-accelerated single-mode light–heavy fluid layers at different Mach numbers: (**a**) maximum vorticity (ω_{max}) and (**b**) minimum vorticity (ω_{min}).

Circulation serves as a fundamental diagnostic for quantifying the strength and evolution of vortical structures in shock-driven flows. In the context of instability growth, it provides a direct measure of the baroclinically generated vortices deposited at the perturbed interface and reflects the balance between counter-rotating motions. The total circulation in the flow field is defined as the spatial integral of vorticity over the computational domain D:

$$\Gamma_{Tot}(t) = \int_D \omega \, dx \, dy. \tag{18}$$

For a more detailed characterization, circulation can be decomposed into its positive and negative components, representing the contributions of oppositely rotating vortical regions:

$$\Gamma_{Pos}(t) = \int_{D,\omega>0} \omega \, dx \, dy, \qquad \Gamma_{Neg}(t) = \int_{D,\omega<0} \omega \, dx \, dy. \tag{19}$$

Here, $\Gamma_{Pos}(t)$ and $\Gamma_{Neg}(t)$ track the temporal evolution of clockwise and counterclockwise vortical structures, respectively, while their sum yields the net circulation $\Gamma_{Tot}(t)$. Together, these diagnostics provide an integrated measure of baroclinic vorticity deposition, allowing us to assess both the individual contributions of counter-rotating regions and the overall rotational strength in the shocked stratification.

Figure 20 shows the temporal evolution of spatially integrated circulation in shock-accelerated light–heavy fluid layers for various Mach numbers. The positive and negative circulations, Γ_{Pos} and Γ_{Neg}, represent counter-rotating vortices, while their sum gives the net circulation Γ_{Tot}. At low Mach numbers ($M_s = 1.15$–1.25), both components remain weak, yielding near-zero net circulation. With increasing M_s, circulation amplifies and Γ_{Neg} dominates, reflecting stronger spike-driven vorticity. For $M_s = 1.50$, circulation peaks correspond to the roll-up of large vortices during nonlinear growth. At higher Mach

numbers ($M_s = 1.75$–2.00), both components intensify markedly, but asymmetry between Γ_{Pos} and Γ_{Neg} becomes pronounced and unsteady fluctuations in Γ_{Tot} indicate complex, multi-scale vortex interactions. The results demonstrate that circulation asymmetry increases with Mach number, particularly beyond $M_s = 1.5$, due to uneven baroclinic torque deposition at spike and bubble locations, further reinforced by dilatational amplification near compressed regions. This imbalance critically influences interface morphology and may aid instability suppression, consistent with Zheng et al. [47], who showed that adjusting circulation ratios between counter-rotating vortices can delay roll-up and mitigate interface distortion. Hence, higher Mach numbers naturally enhance circulation imbalance, suggesting a potential pathway for active control through tailored compressibility or shock-focusing patterns.

Enstrophy and kinetic energy serve as key diagnostics for characterizing shock-accelerated instabilities. Enstrophy quantifies the amplification of baroclinically generated vortical structures, while kinetic energy measures the redistribution of bulk flow energy into interface deformation and progressively smaller scales. For a two-dimensional flow, the enstrophy is defined as the spatial integral of the squared vorticity over the computational domain D:

$$\Omega(t) = \int_D \omega^2 \, dx \, dy, \tag{20}$$

which represents the cumulative strength of vortical activity within the flow field. The total kinetic energy in the domain is given by

$$E_k(t) = \int_D \frac{1}{2} \rho \left(u^2 + v^2\right) dx \, dy, \tag{21}$$

providing a global measure of the bulk momentum and its progressive transfer into interface deformation, shear layers, and small-scale vortices. Together, these diagnostics allow us to evaluate both the buildup of rotational structures and the energy cascade that drives the nonlinear growth of RMI.

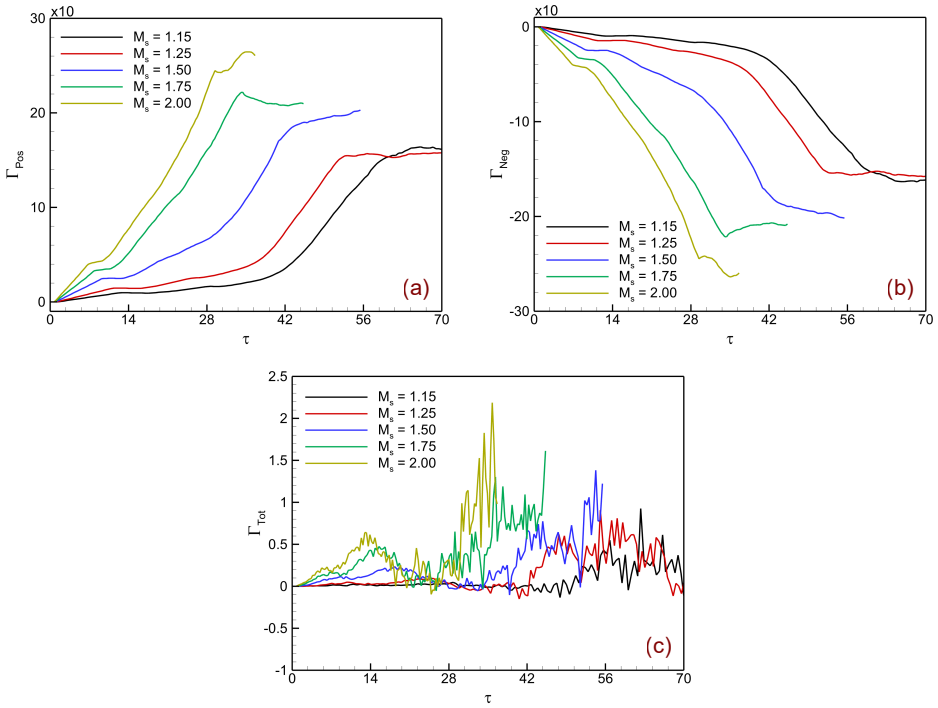

Figure 20. Temporal evolution of spatially integrated circulation in shock-accelerated single-mode light–heavy fluid layers at different Mach numbers: (**a**) positive circulation (Γ_{Pos}), (**b**) negative circulation (Γ_{Neg}), and (**c**) total circulation (Γ_{Tot}).

Figure 21 presents the temporal evolution of spatially integrated enstrophy (Ω) and kinetic energy (E_k) in shock-driven light–heavy fluid layers at different Mach numbers, illustrating the buildup of vortical activity and energy redistribution into interface deformation and small-scale motions. At low Mach numbers ($M_s = 1.15$–1.25), both Ω and E_k remain weak, consistent with limited baroclinic vorticity deposition and gradual interface evolution. For $M_s = 1.50$, the rapid growth of both quantities is observed—enstrophy peaks coincide with vigorous vortex roll-ups, while the increase in E_k reflects efficient conversion of shock energy into shear and rotational motion. At higher Mach numbers ($M_s = 1.75$–2.00), amplification becomes dominant: Ω reaches large magnitudes due to intense vorticity generation, and E_k rises sharply, signifying strong shock focusing, enhanced momentum transfer, and the onset of complex, multi-scale vortical interactions.

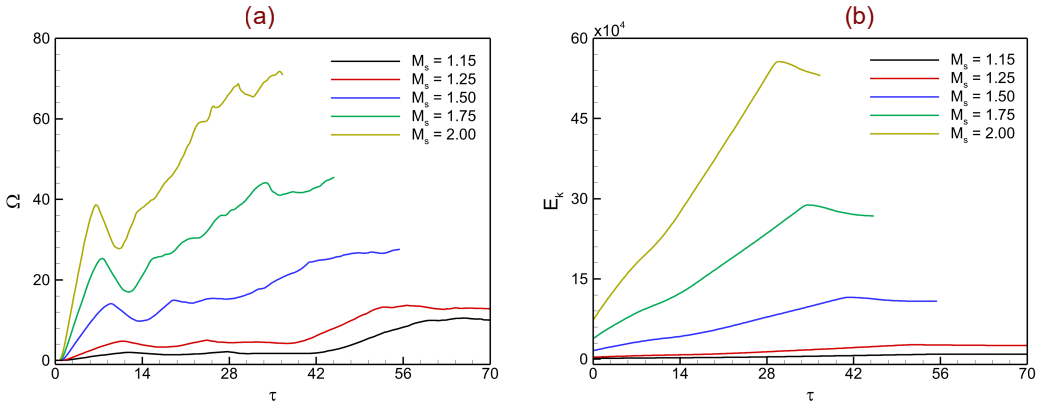

Figure 21. Temporal evolution of spatially integrated fields in shock-accelerated single-mode light–heavy fluid layers at different Mach numbers: (**a**) enstrophy Ω, quantifying the cumulative strength of vortical activity, and (**b**) kinetic energy E_k, measuring the redistribution of bulk momentum into interface deformation and small-scale motions.

5.5. Interface Evolution and Morphological Measures

This section analyzes the evolution of interface morphology in shock-accelerated single-mode light–heavy fluid layers. The diagnostics considered include interface trajectories, normalized interface length, and perturbation amplitude, which together quantify how baroclinic vorticity deposition and successive shock interactions govern interface displacement, deformation, and instability growth. As illustrated schematically in Figure 22, the upstream interface (UI), downstream interface (DI), and transmitted shock (TS1) positions are tracked to measure interface motion, while the amplitude (a) and length (L) parameters describe the geometric evolution of the perturbed interface. These morphological measures provide direct indicators of Mach number effects, capturing both large-scale interface motion and the emergence of fine-scale structures that accelerate the transition to nonlinear mixing.

Figure 23 presents the temporal evolution of the normalized trajectories of the upstream interface ($X^\star_{\mathrm{UI}}$), downstream interface ($X^\star_{\mathrm{DI}}$), and transmitted shock ($X^\star_{\mathrm{TS1}}$) in shock-driven single-mode light–heavy fluid layers for different Mach numbers. The normalization is performed as $X^\star_{\mathrm{UI}} = X_{\mathrm{UI}}/d_{\mathrm{UI}}$, $X^\star_{\mathrm{DI}} = X_{\mathrm{DI}}/d_{\mathrm{DI}}$, and $X^\star_{\mathrm{TS1}} = X_{\mathrm{TS1}}/d_{\mathrm{TS1}}$, where d_{UI}, d_{DI}, and d_{TS1} denote the initial distances of the respective interfaces and the transmitted shock from the incident shock front. All trajectories exhibit an approximately linear increase with nondimensional time, indicating quasi-steady propagation following the initial shock–interface interaction. The propagation rates scale monotonically with M_s, confirming that higher Mach numbers generate stronger post-shock acceleration and greater baroclinic vorticity deposition. The downstream interface lags the upstream interface due to pressure decay and wave attenuation across the heavy layer, whereas the transmitted shock exhibits the highest advancement rate, consistent with enhanced compression and

reduced impedance mismatch at larger M_s values. These results quantitatively establish the Mach-number dependence of interfacial transport and transmitted-shock dynamics in compressible, multi-species layers.

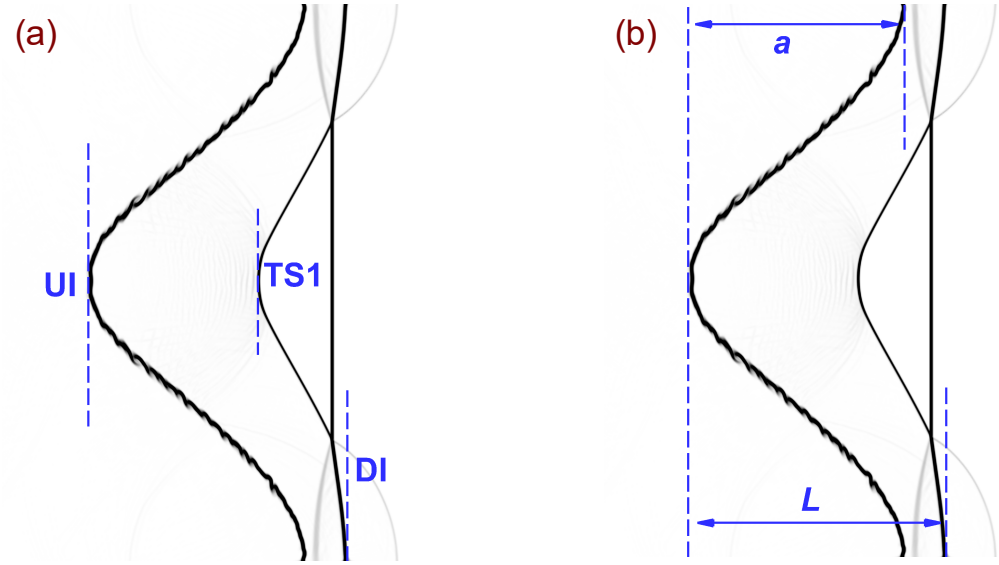

Figure 22. Schematic representation of the interface evolution and morphological diagnostics in a shock-accelerated single-mode light–heavy fluid layer. (**a**) Definition of upstream interface (UI), downstream interface (DI), and transmitted shock (TS1) locations used to track interface displacement. (**b**) Geometric measures of interface deformation, including amplitude (a) and length (L), which quantify perturbation growth and stretching during instability evolution.

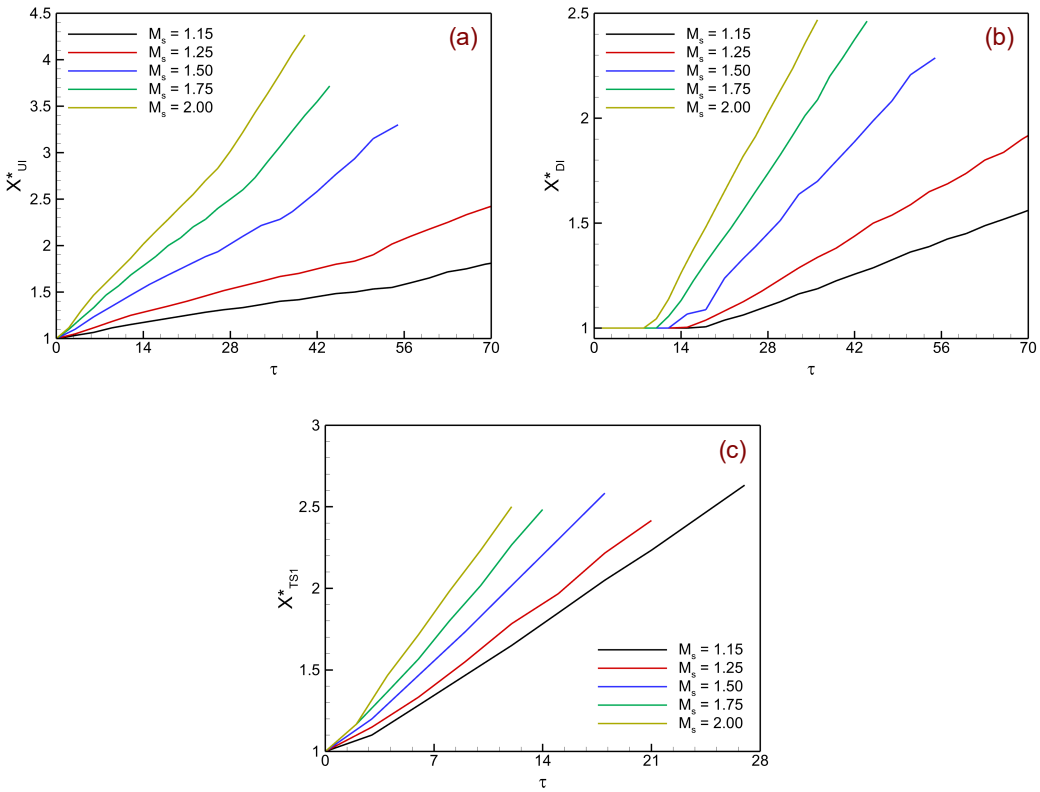

Figure 23. Temporal evolution of normalized interface trajectories in shock-accelerated single-mode light–heavy fluid layers at different Mach numbers: (**a**) upstream interface position ($X^{\star}_{\mathrm{UI}}$), (**b**) downstream interface position ($X^{\star}_{\mathrm{DI}}$), and (**c**) transmitted shock position ($X^{\star}_{\mathrm{TS1}}$).

Figure 24 presents the temporal evolution of the normalized interface length (L^*) and perturbation amplitude (a^*) in shock-accelerated single-mode light–heavy fluid layers for different Mach numbers. The quantities are defined as $L^* = L/L_0$ and $a^* = a/a_0$, where L_0 and a_0 denote the initial interface length and amplitude, respectively. Immediately after shock impact, both L^* and a^* decrease due to transient compression and the realignment of density and pressure gradients across the interface. As the transmitted and reflected waves interact within the heavy layer, baroclinic vorticity deposition drives interface stretching and amplitude amplification, leading to progressive roll-up and deformation. The growth rates of L^* and a^* exhibit a clear Mach-number dependence: higher M_s values induce stronger circulation, enhanced shear, and faster nonlinear growth, while lower M_s cases remain in the quasi-linear regime for longer durations. At $M_s \geq 1.75$, the interface develops sharp spikes, thin bubbles, and fine-scale structures indicative of advanced mixing, whereas at $M_s \leq 1.25$, deformation remains weak and gradual. These trends confirm that, following initial shock compression, the subsequent interface evolution is predominantly governed by Mach-number-driven baroclinic and compressibility effects that accelerate the transition toward nonlinear instability and mixing.

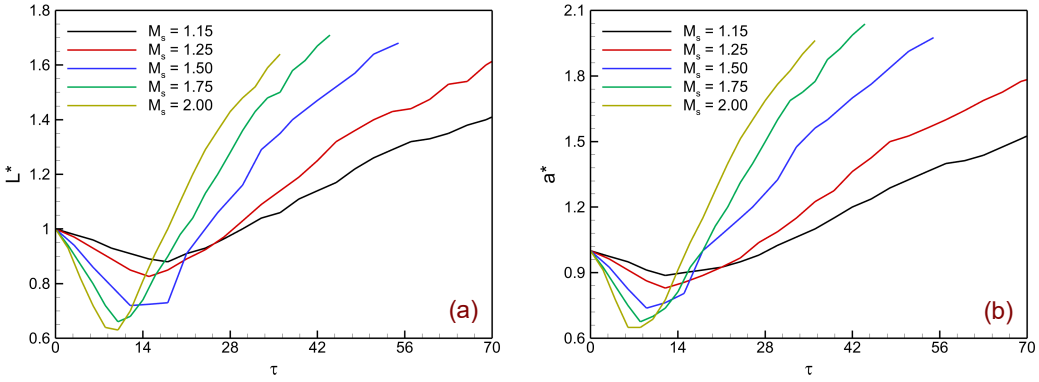

Figure 24. Temporal evolution of normalized interface trajectories in shock-accelerated single-mode light–heavy fluid layers at different Mach numbers: (**a**) normalized interface length (L^*), and (**b**) normalized perturbation amplitude (a^*).

5.6. Influence of Controlling Parameters

The evolution of shock-accelerated interfacial instabilities is strongly influenced by key physical and geometric parameters of the initial configuration. In addition to the shock Mach number, the Atwood number (A), fluid-layer thickness (d), and initial perturbation amplitude (a_0) play decisive roles in determining vorticity generation, interface deformation, and mixing dynamics. The parameters and their respective ranges considered in this analysis are summarized in Table 2. To assess their influence, systematic simulations were conducted by varying these parameters under otherwise identical shock conditions, revealing how density contrast, layer geometry, and perturbation strength jointly control the transition from linear growth to nonlinear mixing.

Table 2. Summary of parameters used to analyze the influence of controlling parameters on shock-accelerated interfacial instabilities. Unless otherwise specified, the wavelength is $\lambda = 100$ mm and the shock Mach number is $M_s = 1.25$.

Controlling Parameter	Symbol	Varied Values	Fixed Parameters	Figure Reference/Description
Atwood number	A	0.30, 0.52, 0.72	$a_0 = 15$ mm, $d = 20$ mm	Figures 25 and 26: Effect of density contrast on instability evolution
Layer thickness	d (mm)	2.5, 10, 40	$A = 0.67$, $a_0 = 15$ mm	Figures 27 and 28: Influence of finite-layer geometry on wave coupling

Table 2. *Cont.*

Controlling Parameter	Symbol	Varied Values	Fixed Parameters	Figure Reference/Description
Initial perturbation amplitude	a_0/λ	0.025, 0.10, 0.40	$A = 0.67$, $d = 20$ mm	Figures 29 and 30: Effect of perturbation strength on nonlinear growth

5.6.1. Effect of Positive Atwood Number

Figure 25 illustrates the influence of the Atwood number (A) on the evolution of shock-accelerated instabilities at a light–heavy fluid layer. For the lowest density contrast ($A = 0.30$; Figure 25a), baroclinic vorticity deposition remains weak, leading to smooth interface deformation characterized by broad bulges and limited roll-up. With an increase to $A = 0.52$ (Figure 25b), stronger density gradients enhance the baroclinic torque, producing more distinct spike–bubble asymmetry and an earlier onset of KH roll-ups. At the highest density contrast ($A = 0.72$; Figure 25c), vorticity generation is substantially amplified, resulting in sharper spikes, thinner bubbles, and vigorous vortex pairing. Hence, increasing the Atwood number intensifies instability growth and accelerates the transition from quasi-linear deformation to strongly nonlinear mixing.

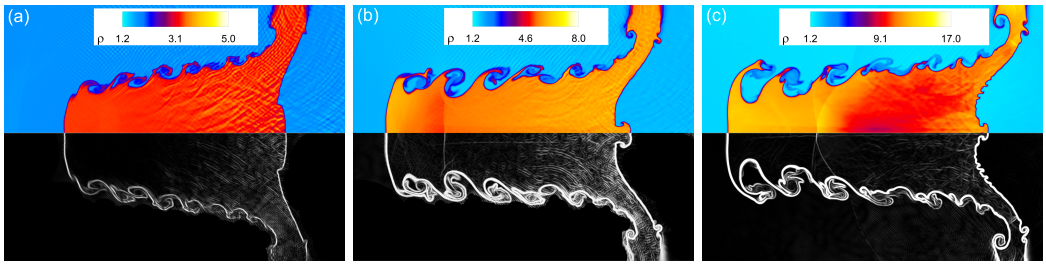

Figure 25. Effects of Atwood number (A) on density contours (upper half) and corresponding Schlieren visualizations (lower half) for a shock-accelerated light–heavy fluid layer at $\tau = 80$: (**a**) $A = 0.30$, (**b**) $A = 0.52$, and (**c**) $A = 0.72$. The incident shock Mach number is $M_s = 1.25$, with initial perturbation amplitude $a_0 = 15$ mm, fluid-layer thickness $d = 20$ mm, and wavelength $\lambda = 100$ mm.

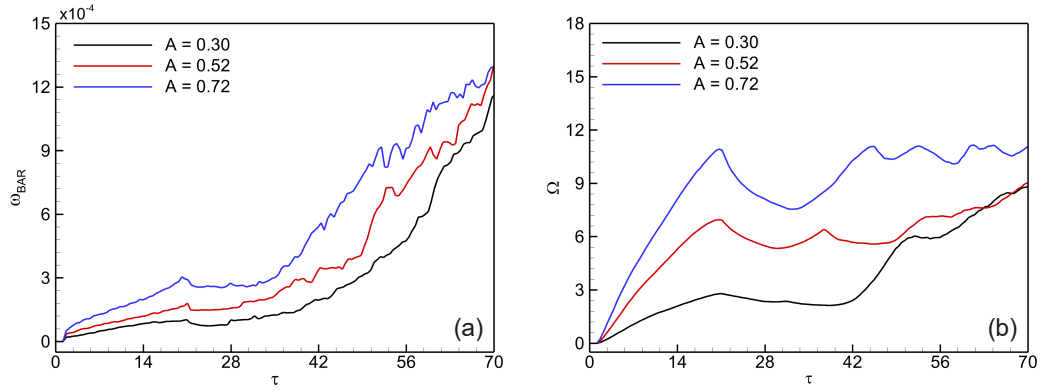

Figure 26. Effects of Atwood number (A) on the temporal evolution of spatially integrated quantities in shock-accelerated single-mode light–heavy fluid layers at $M_s = 1.25$, $a_0 = 15$ mm, $d = 20$ mm, and $\lambda = 100$ mm: (**a**) Baroclinic contribution (ω_{BAR}), and (**b**) enstrophy (Ω).

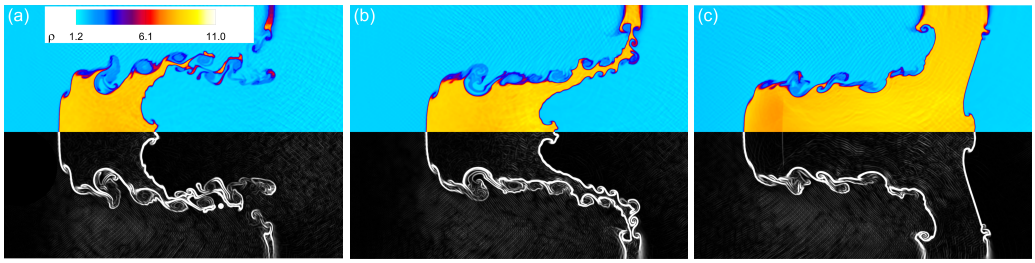

Figure 27. Effects of finite layer thickness (d) on density contours (upper half) and corresponding Schlieren visualizations (lower half) for a shock-accelerated light–heavy fluid layer at $\tau = 80$: (**a**) $d = 2.5$ mm, (**b**) $d = 10$ mm, and (**c**) $d = 40$ mm. The incident shock Mach number is $M_s = 1.25$, with initial perturbation amplitude $a_0 = 15$ mm, Atwood number $A = 0.67$, and wavelength $\lambda = 100$ mm.

Figure 26 further quantifies these effects by depicting the temporal evolution of spatially integrated measures that capture baroclinic vorticity production and enstrophy growth. As shown in Figure 26a, the baroclinic contribution (ω_{BAR}) exhibits a progressive increase over time, with steeper growth for higher A owing to stronger misalignment between pressure and density gradients. This enhanced baroclinic torque yields greater vorticity deposition at the interface. Correspondingly, the enstrophy (Ω) in Figure 26b rises more rapidly for larger A values, reflecting intensified vortical activity and pronounced shear-layer roll-ups. The highest Atwood number case ($A = 0.72$) shows the largest magnitude of both ω_{BAR} and Ω, indicating that stronger density contrast amplifies rotational energy and promotes an earlier transition to nonlinear instability and mixing. Overall, increasing A enhances baroclinic vorticity generation, accelerates interface deformation, and fosters the development of complex multi-scale flow structures.

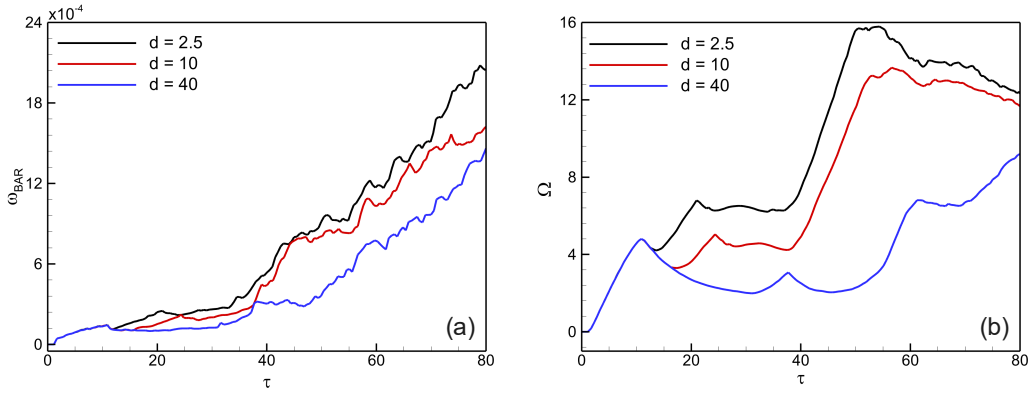

Figure 28. Effects of finite layer thickness (d) on the temporal evolution of spatially integrated quantities in shock-accelerated single-mode light–heavy fluid layers at $M_s = 1.25$, $a_0 = 15$ mm, $A = 0.67$, and $\lambda = 100$ mm: (**a**) baroclinic contribution (ω_{BAR}), and (**b**) enstrophy (Ω).

5.6.2. Effect of Finite Layer Thickness

Figure 27 illustrates the effect of finite layer thickness (d) on the evolution of shock-accelerated instabilities in a light–heavy fluid layer. The thickness of the intermediate heavy layer governs the strength and interaction of transmitted and reflected shocks, thereby influencing baroclinic vorticity deposition and interface morphology. For the thinnest layer ($d = 2.5$ mm; Figure 27a), the close proximity of the two interfaces leads to strong wave coupling and interference, which enhances vorticity generation and promotes rapid interface roll-up. At a moderate thickness ($d = 10$ mm; Figure 27b), the shock interactions within the layer become partially decoupled, resulting in a more symmetric interface structure with balanced spike and bubble development. For the thickest configuration ($d = 40$ mm; Figure 27c), the transmitted shock attenuates before reaching the downstream

interface, reducing baroclinic torque and delaying the onset of secondary instabilities. Thus, thinner layers amplify vorticity deposition and accelerate instability growth through stronger interfacial coupling, whereas thicker layers suppress deformation and postpone the transition to nonlinear mixing.

Figure 28 quantifies these effects by examining the temporal evolution of spatially integrated measures of baroclinic vorticity generation and enstrophy. As shown in Figure 28a, the baroclinic contribution (ω_{BAR}) increases with time for all cases but displays a strong dependence on layer thickness. The thinnest layer ($d = 2.5$ mm) exhibits the largest ω_{BAR}, attributable to enhanced coupling between the upstream and downstream interfaces that intensifies the interaction of transmitted and reflected shocks. For the intermediate layer ($d = 10$ mm), ω_{BAR} remains significant but moderately reduced due to partial decoupling of wave interactions. In contrast, the thickest layer ($d = 40$ mm) shows a gradual increase in ω_{BAR}, indicating weaker baroclinic activity and reduced vorticity deposition. A similar trend is evident in Figure 28b, where the enstrophy (Ω)—representing the cumulative vortical intensity—attains its highest magnitude for the thinnest configuration. The elevated Ω values for small values of d highlight vigorous vortex roll-up and early transition to nonlinear mixing, while thicker layers display delayed and attenuated enstrophy buildup. In summary, decreasing layer thickness enhances baroclinic torque, strengthens vortical activity, and accelerates the instability evolution, whereas increasing d stabilizes the interface and diminishes mixing intensity.

5.6.3. Effect of Initial Perturbation Amplitude

Figure 29 illustrates the effect of initial perturbation amplitude (a_0) on the evolution of shock-accelerated instabilities at a light–heavy fluid layer. The initial interface amplitude governs the strength of baroclinic vorticity deposition and, consequently, the rate of instability growth. For the smallest perturbation ($a_0/\lambda = 0.025$; Figure 29a), the interface deformation remains mild, displaying smooth undulations with delayed roll-up and limited spike–bubble development. When the amplitude increases to $a_0/\lambda = 0.10$ (Figure 29b), the enhanced curvature strengthens the local misalignment between pressure and density gradients, resulting in pronounced spike penetration and the emergence of KH roll-ups. At the largest amplitude ($a_0/\lambda = 0.40$; Figure 29c), the instability rapidly transitions into the nonlinear regime, characterized by sharp spikes, deep bubbles, and vigorous vortex pairing.

Figure 30 quantitatively assesses these effects by examining the temporal evolution of baroclinic vorticity generation and enstrophy for different perturbation amplitudes. As shown in Figure 30a, the baroclinic contribution (ω_{BAR}) increases monotonically with time, with its magnitude strongly dependent on a_0/λ. For the smallest amplitude ($a_0/\lambda = 0.025$), ω_{BAR} remains relatively weak throughout the evolution, indicating minimal interface curvature and reduced misalignment between pressure and density gradients. With a moderate amplitude ($a_0/\lambda = 0.10$), vorticity generation intensifies, producing stronger baroclinic torque and earlier growth of interfacial disturbances. The largest amplitude ($a_0/\lambda = 0.40$) yields the steepest increase in ω_{BAR}, signifying strong vorticity deposition induced by large curvature-driven pressure–density misalignment. A corresponding trend is evident in Figure 30b for enstrophy (Ω), which represents the cumulative vortical energy within the flow. The highest Ω values occur for $a_0/\lambda = 0.40$, confirming that larger initial perturbations enhance rotational energy and accelerate the transition to nonlinear mixing. In contrast, smaller amplitudes lead to delayed enstrophy buildup and slower instability evolution. In summary, increasing a_0 strengthens baroclinic vorticity production, promotes greater vortical activity, and hastens the onset of nonlinear instability growth in shock-driven light–heavy fluid layers.

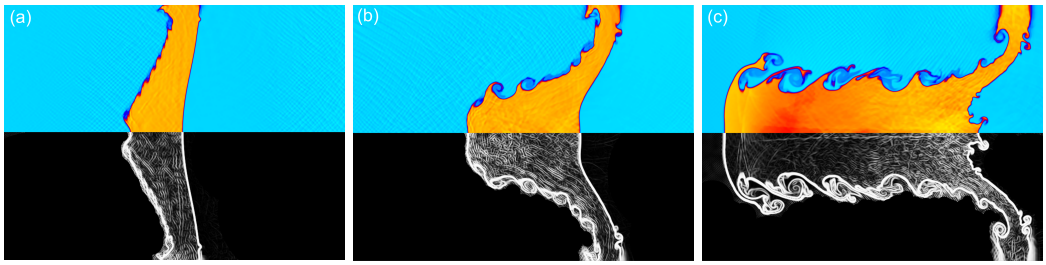

Figure 29. Effects of initial perturbation amplitude (a_0) on density contours (upper half) and corresponding Schlieren visualizations (lower half) for a shock-accelerated light–heavy fluid layer at $\tau = 80$: (**a**) $a_0/\lambda = 0.025$, (**b**) $a_0/\lambda = 0.1$, and (**c**) $a_0/\lambda = 0.4$. The incident shock Mach number is $M_s = 1.25$, with finite layer thickness $d = 20$ mm, Atwood number $A = 0.67$, and wavelength $\lambda = 100$ mm.

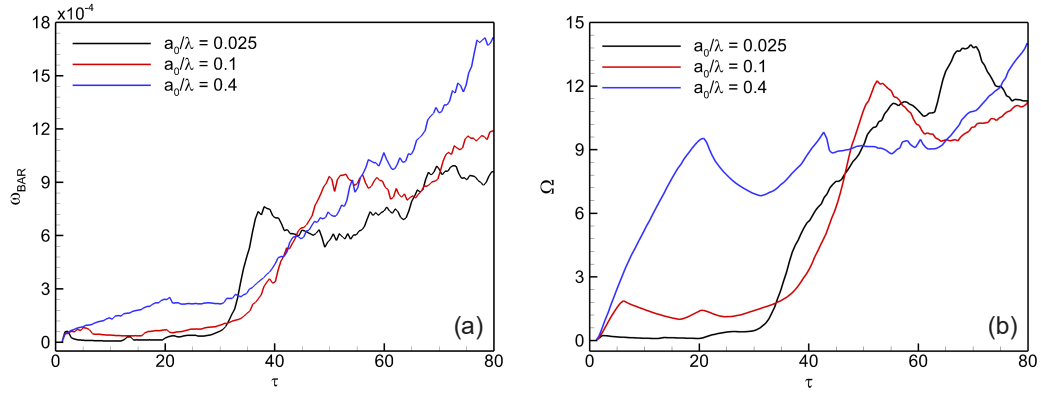

Figure 30. Effects of initial perturbation amplitude (a_0) on the temporal evolution of spatially integrated quantities in shock-accelerated single-mode light–heavy fluid layers at $M_s = 1.25$, $d = 20$ mm, $A = 0.67$, and $\lambda = 100$ mm: (**a**) baroclinic contribution (ω_{BAR}), and (**b**) enstrophy (Ω).

6. Conclusions and Outlook

In this work, we presented a systematic numerical investigation of shock-accelerated instability evolution at a light–heavy fluid layer, focusing on the influence of the incident shock Mach number. The study employed a high-order modal discontinuous Galerkin (DG) framework to solve the two-dimensional compressible multi-species Euler equations, allowing accurate resolution of shocks, interfaces, and small-scale vortical features while isolating the essential inviscid mechanisms of baroclinic vorticity generation and compressibility effects.

The results demonstrate that increasing the Mach number significantly amplifies baroclinic vorticity deposition, accelerates the onset of KH roll-up, and intensifies nonlinear interface deformation. At low Mach numbers, the interface evolves smoothly with delayed instability growth, whereas at higher Mach numbers, the flow transitions into a strongly nonlinear, multi-scale vortical regime characterized by sharp spike thinning, bubble elongation, and complex vortical interactions. Quantitative diagnostics—including circulation, enstrophy, and vorticity extrema—consistently demonstrate the strong Mach number dependence of instability growth. Baroclinic torque was confirmed as the dominant mechanism of vorticity generation across all cases, while compressibility-related dilatation effects become non-negligible at stronger shocks. Furthermore, the inclusion of the influence of controlling parameters extends the parametric understanding of shock-driven instabilities. Comparative analyses across Atwood number, layer thickness, and initial perturbation amplitude reveal their coupled influence on instability evolution. Collectively, these parameters delineate the multidimensional physical space that governs instability amplification, morphological transitions, and the overall dynamics of shock-driven mixing.

Beyond the canonical configuration studied here, the numerical insights are directly relevant to high-speed flow applications such as scramjet combustion and ICF. In scramjets, similar shock–shear interactions govern fuel–air mixing efficiency, while in ICF, shock-driven mixing at ablator–fuel interfaces affects ignition performance. The observed Mach-dependent balance between baroclinic and dilatational effects thus provides a framework for modeling and optimizing such processes. Recent developments by Tang et al. [46] and Zheng et al. [47] demonstrate promising hybrid numerical methods and flow-control strategies that could be integrated into future high-fidelity DG simulations to enhance predictive accuracy and mixing control in practical compressible flow systems.

The present simulations are based on a two-dimensional inviscid formulation, which neglects viscosity, molecular diffusion, and thermal conduction. As such, the model does not capture dissipation, vortex stretching, or three-dimensional cascade mechanisms that govern physical turbulence. Therefore, while the results reveal a transition toward increasingly complex and irregular vortical dynamics at high Mach numbers, they do not represent true turbulent mixing. Instead, the findings provide physically consistent insights into how baroclinic and compressibility-driven effects govern instability amplification and morphological transition in the inviscid limit. Future work will focus on extending the present framework to include viscous (Navier–Stokes) and three-dimensional effects to capture vortex stretching and dissipative dynamics. Systematic studies addressing interface thickness, Atwood number variation, and multimode perturbations will further generalize the results.

Author Contributions: Conceptualization, S.S.; Software, S.S.; Validation, S.S.; Formal analysis, S.S.A. and S.S.; Investigation, S.S.A., S.S., and N.F.A.; Writing—original draft, S.S.A., S.S., and N.F.A.; Visualization, S.S.A. and S.S.; Funding acquisition, S.S.A. All authors have read and agreed to the published version of the manuscript.

Funding: This work was funded by the Deanship of Graduate Studies and Scientific Research at Jouf University under Grant No. DGSSR-2025-FC-01034.

Data Availability Statement: The processed simulation data supporting the findings of this study—including time-series diagnostics of flow fields and representative field snapshots—will be made publicly available in an open-access repository (e.g., Zenodo) upon final acceptance of the manuscript. Additional data and visualization files (Schlieren images) are available from the corresponding author upon reasonable request.

Conflicts of Interest: The authors declare no conflicts of interest.

References

1. Brouillette, M. The Richtmyer-Meshkov instability. *Annu. Rev. Fluid Mech.* **2002**, *34*, 445. [CrossRef]
2. Richtmyer, R.D. Taylor instability in shock acceleration of compressible fluids. *Commun. Pure Appl. Math.* **1960**, *13*, 297–319. [CrossRef]
3. Meshkov, E.E. Instability of the interface of two gases accelerated by a shock wave. *Commun. Pure Appl. Math.* **1969**, *4*, 101. [CrossRef]
4. Zhou, Y. Rayleigh–Taylor and Richtmyer–Meshkov instability induced flow, turbulence, and mixing. I. *Phys. Rep.* **2017**, *720*, 1–136.
5. Zhou, Y. Rayleigh–Taylor and Richtmyer–Meshkov instability induced flow, turbulence, and mixing. II. *Phys. Rep.* **2017**, *723*, 1–160. [CrossRef]
6. Zhou, Y.; Williams, R.J.R.; Ramaprabhu, P.; Groom, M.; Thornber, B.; Hillier, A.; Mostert, W.; Rollin, B.; Balachandar, S.; Powell, P.D.; et al. Rayleigh–Taylor and Richtmyer–Meshkov instabilities: A journey through scales. *Phys. D Nonlinear Phenom.* **2021**, *423*, 132838. [CrossRef]
7. Zhou, Y.; Sadler, J.D.; Hurricane, O.A. Instabilities and mixing in inertial confinement fusion. *Annu. Rev. Fluid Mech.* **2025**, *57*, 197–225. [CrossRef]
8. Prime, M.B.; Fensin, S.J.; Jones, D.R.; Dyer, J.W.; Martinez, D.T. Multiscale Richtmyer-Meshkov instability experiments to isolate the strain rate dependence of strength. *Phys. Rev. E* **2024**, *109*, 015002. [CrossRef]
9. Betti, R.; Hurricane, O.A. Inertial-confinement fusion with lasers. *Nat. Phys.* **2016**, *12*, 435–448. [CrossRef]

10. Kuranz, C.C.; Park, H.-S.; Huntington, C.M.; Miles, A.R.; Remington, B.A.; Plewa, T.; Trantham, M.R.; Robey, H.F.; Shvarts, D.; Shimony, A.; et al. How high energy fluxes may affect Rayleigh–Taylor instability growth in young supernova remnants. *Nat. Commun.* **2018**, *9*, 1564. [CrossRef]
11. Urzay, J. Supersonic combustion in air-breathing propulsion systems for hypersonic flight. *Annu. Rev. Fluid Mech.* **2018**, *50*, 593–627. [CrossRef]
12. Li, L.; Jin, T.; Zou, L.; Luo, K.; Fan, J. Numerical study of Richtmyer-Meshkov instability in finite thickness fluid layers with reshock. *Phys. Rev. E* **2024**, *109*, 055105. [CrossRef] [PubMed]
13. Schill, W.J.; Armstrong, M.R.; Nguyen, J.H.; Sterbentz, D.M.; White, D.A.; Benedict, L.X.; Rieben, R.N.; Hoff, A.; Lorenzana, H.E.; Belof, J.L.; et al. Suppression of Richtmyer-Meshkov instability via special pairs of shocks and phase transitions. *Phys. Rev. Lett.* **2024**, *132*, 024001. [CrossRef] [PubMed]
14. Zhou, Y. *Hydrodynamic Instabilities and Turbulence: Rayleigh–Taylor, Richtmyer–Meshkov, and Kelvin–Helmholtz Mixing*; Cambridge University Press: Cambridge, UK, 2024.
15. Youngs, D.L. Numerical simulation of turbulent mixing by Rayleigh-Taylor instability. *Phys. D Nonlinear Phenom.* **1984**, *12*, 32–44. [CrossRef]
16. Dimotaki, P.E. Turbulent mixing. *Annu. Rev. Fluid Mech.* **2005**, *37*, 329–356. [CrossRef]
17. Samtaney, R.; Pullin, D.I. On initial-value and self-similar solutions of the compressible Euler equations. *Phys. Fluids* **1996**, *8*, 2650–2655. [CrossRef]
18. Velikovich, A.L.; Dimonte, G. Nonlinear perturbation theory of the incompressible Richtmyer-Meshkov instability. *Phys. Rev. Lett.* **1996**, *76*, 3112. [CrossRef]
19. Singh, S. Contribution of Mach number to the evolution of the Richtmyer-Meshkov instability induced by a shock-accelerated square light bubble. *Phys. Rev. Fluids* **2021**, *6*, 104001. [CrossRef]
20. Singh, S.; Battiato, M. Numerical investigation of shock Mach number effects on Richtmyer–Meshkov instability in a heavy square bubble. *Phys. D Nonlinear Phenom.* **2023**, *453*, 133844. [CrossRef]
21. Lombardini, M.; Pullin, D.I.; Meiron, D.I. Transition to turbulence in shock-driven mixing: A Mach number study. *J. Fluid Mech.* **2012**, *690*, 203–226. [CrossRef]
22. Braun, N.O.; Pullin, D.I.; Meiron, D.I. Large eddy simulation investigation of the canonical shock–turbulence interaction. *J. Fluid Mech.* **2019**, *858*, 500–535. [CrossRef]
23. Rikanati, A.; Oron, D.; Sadot, O.; Shvarts, D. High initial amplitude and high Mach number effects on the evolution of the single-mode Richtmyer-Meshkov instability. *Phys. Rev. E* **2003**, *67*, 026307. [CrossRef] [PubMed]
24. Quirk, J.J.; Karni, S. On the dynamics of a shock–bubble interaction. *J. Fluid Mech.* **1996**, *318*, 129–163. [CrossRef]
25. Haas, J.F.; Sturtevant, B. Interaction of weak shock waves with cylindrical and spherical gas inhomogeneitiesn. *J. Fluid Mech.* **1987**, *181*, 41–76. [CrossRef]
26. Gowardhan, A.A.; Grinstein, F.F. Numerical simulation of Richtmyer–Meshkov instabilities in shocked gas curtains. *J. Turbul.* **2011**, *12*, N43. [CrossRef]
27. Singh, S.; Battiato, M.; Myong, R.S. Impact of bulk viscosity on flow morphology of shock-accelerated cylindrical light bubble in diatomic and polyatomic gasess. *Phy. Fluids* **2021**, *33*, 066103. [CrossRef]
28. Chen, Y.; Jin, T.; Zou, L. Numerical study of Richtmyer–Meshkov instability in shocked composite curtain under different initial conditions. *Phy. Fluids* **2025**, *37*, 034106. [CrossRef]
29. Mikaelian, K.O. Numerical simulations of Richtmyer–Meshkov instabilities in finite-thickness fluid layers. *Phy. Fluids* **1996**, *8*, 1269–1292. [CrossRef]
30. Msmali, A.H.; Singh, S.; Meetei, M.Z. Single-Mode Richtmyer–Meshkov Instability in Light Fluid Layer: Insights from Numerical Simulations. *Axioms* **2025**, *14*, 473. [CrossRef]
31. Zhang, D.; Ding, J.; Si, T.; Luo, X. Divergent Richtmyer–Meshkov instability on a heavy gas layer. *J. Fluid Mech.* **2023**, *959*, A37. [CrossRef]
32. Lindl, J. Development of the indirect-drive approach to inertial confinement fusion and the target physics basis for ignition and gain. *Phy. Plasmas* **1995**, *2*, 3933–4024. [CrossRef]
33. Alsaeed, S.S.; Satyvir, S.; Alrubea, N.A. Numerical investigation of Atwood number effects on shock-driven single-mode stratified heavy fluid layers. *Mathematics* **2025**, *13*, 3032. [CrossRef]
34. Alsaeed, S.S.; Satyvir, S.; Alrubea, N.A. Layer thickness impact on shock-accelerated interfacial instabilities in single-mode stratifications. *Appl. Sci.* **2025**, *15*, 10687. [CrossRef]
35. Jacobs, J.W.; Krivets, V.V. Experiments on the late-time development of single-mode Richtmyer–Meshkov instability. *Phy. Fluids* **2005**, *17*, 034105. [CrossRef]
36. Holmes, R.L.; Dimonte, G.; Fryxell, B.; Gittings, M.L.; Grove, J.W.; Schneider, M.; Sharp, D.H.; Velikovich, A.L.; Weaver, R.P.; Zhang, Q. Richtmyer–Meshkov instability growth: Experiment, simulation and theory. *J. Fluid Mech.* **1999**, *389*, 55–79. [CrossRef]

37. Singh, S.; Battiato, M. Numerical simulations of Richtmyer–Meshkov instability of SF6 square bubble in diatomic and polyatomic gases. *Comput. Fluids* **2022**, *242*, 105502. [CrossRef]
38. Anuchina, N.N.; Volkov, V.I.; Gordeychuk, V.A.; Es' kov, N.S.; Ilyutina, O.S.; Kozyrev, O.M. Numerical simulations of Rayleigh–Taylor and Richtmyer–Meshkov instability using MAH-3 code. *J. Comput. Appl. Math.* **2004**, *168*, 11–20. [CrossRef]
39. Tapinou, K.C.; Wheatley, V.; Bond, D.; Jahn, I. The Richtmyer–Meshkov instability of thermal, isotope and species interfaces in a five-moment multi-fluid plasma. *J. Fluid Mech.* **2022**, *951*, A11. [CrossRef]
40. Sashi Kumar, G.N.; Maheshwari, N.K. A lattice Boltzmann method for simulation of multi-species shock accelerated flows. *Int. J. Comut. Fluid Dyn.* **2018**, *32*, 19–34. [CrossRef]
41. Cockburn, B.; Shu, C.-W. The Runge–Kutta discontinuous Galerkin method for conservation laws V: Multidimensional systems. *J. Comput. Phys.* **1998**, *141*, 199–224. [CrossRef]
42. Krivodonova, L.; Xin, J.; Remacle, J.F.; Chevaugeon, N.; Flaherty, J.E. Shock detection and limiting with discontinuous Galerkin methods for hyperbolic conservation laws. *App. Num. Math.* **2004**, *48*, 323–338. [CrossRef]
43. Singh, S.; Karchani, A.; Chourushi, T.; Myong, R.S. A three-dimensional modal discontinuous Galerkin method for the second-order Boltzmann-Curtiss-based constitutive model of rarefied and microscale gas flows. *J. Comput. Phys.* **2022**, *457*, 111052. [CrossRef]
44. Wang, Z.; Yao, K.; Chang, J.; Yue, L.; Chen, H.; Huang, R.; Chao, Y. Experimental investigation of shock-wave–streamwise-vortex interaction. *AIAA J.* **2025**, *63*, 3079–3106. [CrossRef]
45. Wang, Z.; Yao, K.; Xin, X.; Huang, R.; Chang, J. Experimental and numerical simulation of shock train characteristics in the concave channel. *J. Propuls. Power* **2025**, *41*, 602–623. [CrossRef]
46. Tang, Y.; Wei, X.; Liu, Y. Hybrid RANS-LES simulation of rotor–stator interaction in a compressor stage using a grid-adaptive simulation method. *J. Turbomach.* **2025**, *147*, 071001. [CrossRef]
47. Tang, Y.; Wei, X.; Liu, Y. einforcement learning-based plasma flow control of asymmetric vortices over a slender body at high angles of attack. *Phys. Fluids* **2025**, *37*, 035138.
48. Fujio, C.; Ogawa, H. Optimization and data mining for shock-induced mixing enhancement inside scramjet using stochastic deep-learning flowfield prediction. *Aerosp. Sci. Technol.* **2025**, *154*, 109513. [CrossRef]
49. Peng, S.; Chen, Q. Hypermixer induced shock-vortex-plume interaction and mixing enhancement in a high Mach number supersonic flow. *Phys. Fluids* **2025**, *37*, 096128. [CrossRef]
50. Singh, S. Investigation of aspect ratio effects on flow characteristics and vorticity generation in shock-induced rectangular bubble. *Eur. J. Mech. B Fluids* **2023**, *101*, 131–148. [CrossRef]
51. Johnsen, E.; Colonius, T. Implementation of WENO schemes in compressible multicomponent flow problems. *J. Comput. Phys.* **2006**, *219*, 715–732. [CrossRef]
52. Gottlieb, S.; Shu, C.-W.; Tadmor, E. Strong stability-preserving high-order time discretization methods. *SIAM Rev.* **2001**, *43*, 89–112. [CrossRef]
53. Luo, X.; Dong, P.; Si, T.; Zhai, Z. The Richtmyer–Meshkov instability of a 'V'shaped air/SF_6 interface. *J. Fluid Mech.* **2016**, *802*, 186–202. [CrossRef]
54. Ou, J.; Zhai, Z. Effects of aspect ratio on shock-cylinder interaction. *Acta Mech. Sin.* **2019**, *35*, 61–69. [CrossRef]